Astronomy & Astrophysics manuscript no. M17_IRS5_v8
February 18, 2015

©ESO 2015

arXiv:1502.04959v1 [astro-ph.GA] 17 Feb 2015

VLT near- to mid-IR imaging and spectroscopy of the M 17 UC1 – IRS5 region ⋆

Zhiwei Chen[1, 2, 3], Dieter E. A. Nürnberger[2], Rolf Chini[2, 4], Zhibo Jiang[1], and Min Fang[1]

[1] Purple Mountain Observatory & Key Laboratory for Radio Astronomy, Chinese Academy of Sciences, 2 West Beijing Road, 210008 Nanjing, China
e-mail: `zwchen@pmo.ac.cn`
[2] Astronomisches Institut, Ruhr–Universität Bochum, Universitätsstrasse 150, 44801 Bochum, Germany
[3] University of Chinese Academy of Sciences, 100039 Beijing, China
[4] Instituto de Astronomía, Universidad Católica del Norte, Avenida Angamos 0610, Casilla 1280 Antofagasta, Chile

Received date; accepted date

ABSTRACT

Aims. We investigate the surroundings of the hypercompact H ɪɪ region M 17 UC1 to probe the physical properties of the associated young stellar objects and the environment of massive star formation.

Methods. We use diffraction-limited near-IR (VLT/NACO) and mid-IR (VLT/VISIR) images to reveal the different morphology at various wavelengths. Likewise we investigate the stellar and nebular content of the region by VLT/SINFONI integral field spectroscopy with a resolution $R \sim 1500$ at $H + K$ bands.

Results. Five of the seven point sources in this region show L-band excess emission. Geometric match is found between the H_2 emission and near-IR polarized light in the vicinity of IRS5A, and between the diffuse mid-IR emission and near-IR polarization north of UC1. The H_2 emission is typical for dense PDRs, which are FUV pumped initially and repopulated by collisional de-excitation. The co-presence of He ɪ, H ɪ, and H_2 lines in most region argues against an edge-on configuration of the M 17 SW PDR, but is in favor of a moderately inclined geometry with respect to the line of sight. The spectral types of IRS5A and B273A are B3−B7 V/III and G4−G5 III, respectively. The observed infrared luminosity L_{IR} in the range $1 - 20\,\mu$m is derived for three objects; we obtain $2.0 \times 10^3\,L_\odot$ for IRS5A, $13\,L_\odot$ for IRS5C, and $10\,L_\odot$ for B273A.

Conclusions. IRS5 might be a young quadruple system. Its primary star IRS5A is confirmed to be a high-mass protostellar object ($\sim 9\,M_\odot, \sim 1 \times 10^5$ yrs); it might have terminated accretion due to the feedback from the stellar activities (radiation pressure, outflow) and the expanding H ɪɪ region of M 17. UC1 might also have terminated accretion because of the expanding hypercompact H ɪɪ region ionized by itself. The disk clearing process of the low-mass YSOs in this region might be accelerated by the expanding H ɪɪ region. The outflows driven by UC1 are running in south-north with its northeastern side suppressed by the expanding ionization front of M 17; the blue-shifted outflow lobe of IRS5A is seen in two types of tracers along the same line of sight in the form of H_2 emission filament and mid-emission. The H_2 line ratios probe the properties of M 17 SW PDR, which is confirmed to have a clumpy structure with two temperature distributions: warm, dense molecular clumps with $n_{\mathrm{H}} > 10^5\,\mathrm{cm}^{-3}$ and $T \approx 575\,\mathrm{K}$ and cooler atomic gas with $n_{\mathrm{H}} \sim 3.7 \times 10^3 - 1.5 \times 10^4\,\mathrm{cm}^{-3}$ and $T \sim 50 - 200\,\mathrm{K}$.

Key words. stars: early-type –stars: formation –stars: individual: M 17 UC1 –ISM: individual objects: M 17 SW –ISM: molecules: photon-dominated region (PDR)

1. Introduction

Massive stars ($> 8\,M_\odot$) affect their surroundings by ionizing radiation and strong stellar winds throughout their life, as well as by metal enrichment in their final fate as Supernovae. However, the formation process of massive stars is still a hot open debate. Both theoretical prediction and observational evidence suggest that massive stars most likely form via accretion of material quite similar to low-mass stars, but the involved processes may not be only simply scaled up (Zinnecker & Yorke 2007, and references therein). The major difference is the energetic feedback (radiation pressure, stellar winds and outflows) which rapidly dissipates the circumstellar envelope and consequently limits the mass growth of the central young stellar object (YSO). In addition, for high-mass YSOs the earliest evolutionary phase (protostellar phase, before reaching the zero-age main sequence, hereafter ZAMS) is very short, as characterized by Kelvin-Helmholtz timescales of less than 10^5 yrs. Thus, massive stars evolve fast, even during their accretion phase. It is thought that the time spent in the main accretion phase might be significantly less than the main-sequence lifetime, presumably of the order of a few dynamical times of the star-forming molecular core. Therefore, to accumulate sufficiently large amounts of material during the very short timescale, accretion rates of high-mass YSOs must be much higher than those of low-mass YSOs, e.g., $\gtrsim 10^{-4}\,M_\odot\,\mathrm{yr}^{-1}$ (e.g. Hosokawa et al. 2010, hereafter H+10) compared with $< 10^{-8}\,M_\odot\,\mathrm{yr}^{-1}$ (e.g. Fang et al. 2013). The strong feedback from massive protostars may prevent the accretion even before the arrival at the ZAMS if accretion rates are constantly larger than a few $10^{-3}\,M_\odot\,\mathrm{yr}^{-1}$. This settles an upper limit for the protostars around several tens of solar masses. In fact, accretion rates may vary strongly with the evolution of massive protostars. Massive accretion might continue in a non-

---

⋆ Based on observations by the European Southern Observatory Very Large Telescope on Cerro Paranal, Chile (ESO program IDs: 281.C-5027(A), 281.C-5051(A,B)) steady fashion, which potentially allows even more massive stars to form by mass accretion (H+10).

The evolution of massive protostars at such high accretion rates is still the vague feature of massive star formation which determines the feedback on their environment. Numerical simulations show that accreting massive protostars with high accretion rates have large radius. For instance, at an accretion rate of $1 \times 10^{-3}\,M_{\odot}\,\mathrm{yr}^{-1}$, the protostellar radius may exceed $100\,R_{\odot}$ at maximum (e.g. Yorke & Bodenheimer 2008; Hosokawa & Omukai 2009). Such a large radius hence leads to low effective temperature, and very low stellar UV luminosity, which might be too low for the growth of an H II region around the protostar (Churchwell 2002; Keto 2007; Murphy et al. 2010). High-mass protostars are considered to precede the formation of an H II region. From the observational view, a lot of high-mass protostar candidates have high infrared luminosities without observable H II regions (Kumar & Grave 2007; Molinari et al. 2008; Grave & Kumar 2009).

Sect. 2 briefly introduces the massive star-forming region M 17, and particularly summarizes the studies of the M 17 UC – IRS5 region. In Sect. 3, the observations and data reduction are described. The results based on near- to mid-IR data are presented in Sect. 4. The derived properties are discussed in Sect. 5, and the conclusions are presented in Sect. 6.

2. M 17 UC1 – and the southwestern photodissociation region

In a distance of $1.98^{+0.14}_{-0.12}$ kpc (Xu et al. 2011), M 17 is among the best laboratories in the Galaxy for investigating the formation of massive stars. In this paper, we report near- to mid-IR imaging and integral-field spectroscopic studies for the M 17 UC1 – IRS5 region (see Fig. 1), which is located just west of the arc-like ionization front (IF). This region is well known because of the hypercompact H II (HCHIIregion M 17 UC1 (Sewilo et al. 2004), which is surrounded by a circumstellar disk (Nielbock et al. 2007, hereafter N+07). The other interesting object, M 17 IRS5, is a bright IR source located 5″ southwest of M 17 UC1; in contrast to the HCHII region it is not detectable at 1.3 cm (Chini et al. 2000). Its spectral energy distribution (SED) at IR wavelengths suggests a warmer component with color temperature ∼ 1000 K, and a cooler component ∼ 150 K (Nielbock et al. 2001, hereafter N+01). The non-detection of an associated H II region is reminiscent of the early protostellar phase when the protostar is huge with low effective temperature and low UV luminosity – meaning that IRS 5 might be younger than UC1. However, this explanation is just one of the three plausible scenarios proposed by Kassis et al. (2002) (hereafter K+02). An H II region with a density higher than $3 \times 10^{5}\,\mathrm{cm}^{-3}$ or a heavy dusty envelope could also escape detection. Previous near-IR polarization studies revealed infrared reflection nebulae (IRN) associated with the two sources (Chen et al. 2012, hereafter CZ+12), which might trace potential outflows. The third bright IR source, M 17 B273, projected against the edge of the arc-shaped IF, might be a YSO too (near-IR excess, see Hanson et al. 1997), but requires a spectroscopic classification.

Besides characterizing the stellar content, the SINFONI integral-field spectroscopy can also be used to investigate the diffuse nebular emission of M 17 SW – one of the best-studied dense PDRs in the Galaxy. At far-IR to millimeter wavelengths, studies of molecular and atomic emission indicate that the structure of the gas is highly clumped (Stutzki et al. 1988; Stutzki & Guesten 1990; Meixner et al. 1992; Pérez-Beaupuits et al. 2010), and supported by magnetic field rather than by thermal gas pressure (Pellegrini et al. 2007). Temperatures of ∼ 275 K were found toward the IF (Brogan & Troland 2001). One characteristic of PDRs is H_2 emission originating from the collisional deexcitation of H_2 molecules initially excited by UV photons, which is an important heating mechanism of dense PDRs (Sternberg & Dalgarno 1989). Sheffer & Wolfire (2013) reported four mid-IR pure-rotational H_2 lines toward M 17 SW which are consistent with H_2 emission in high-density clumps ($n_{\mathrm{H}} > 10^{5}\,\mathrm{cm}^{-3}$) embedded in an interclump atomic gas of density lower by two or three orders of magnitude (Meixner et al. 1992; Meixner & Tielens 1993). Nürnberger et al. (2007) reported near-IR H_2 emission associated with a jet ejected by a forming high-mass protostar, which is just located 1′ southeast to the M 17 UC1 – IRS5 region. In such case, H_2 emission is produced by thermal emission in shock fronts.

3. Observations and data reduction

3.1. SINFONI observations

High spatial resolution (AO supported), middle spectral resolution ($R \sim 1500$) near-IR integral field spectroscopic data of the M 17 UC1 – IRS5 region (see Fig. 1) were taken in Service Mode during the nights 2008-06-08/09, 2008-09-26/27 and 2008-09-27/28, using ESO's near-IR integral field spectrograph SINFONI (**S***pectrograph for* **IN***tegral* **F***ield* **O***bservations in the* **N***ear-***I***nfrared*; Gillessen et al. 2005) mounted on the Cassegrain focus of the VLT Yepun at the Paranal observatory, Chile.

Overall, we observed a sequence of 4 adjacent target positions (see Table 1). In all cases, AO curvature sensing was performed on the reference source M17-CEN 64 (RA = 18:20:25.71, DEC = −16:11:41.7, J2000), which is located at the distance of about 16.″5 toward the east of IRS5 (about 12″ toward the south-east of B273). For appropriate sky subtraction, a nearby empty sky position was available at the distance of about 70″ – 90″ toward the west of IRS5.

In a trade-off between avoiding saturation of the spectra of the central point source and optimizing both dynamic range and field of view (FOV) for the diffuse circumstellar emission, we set up SINFONI with its 100 mas pixel scale, covering an instantaneous FOV of about 3″ × 3″ with 64 × 32 pixels of 50 mas × 100 mas each, together with the $H + K$ grating, which comprises the wavelength range from about 1.45 μm to 2.45 μm at the spectral resolution of about 1.0 nm (dispersion of 0.50 nm/pixel). The detector integration times (DITs) were set to 60 s (with NDIT = 1), both for on-source (science) exposures and off-source (sky) exposures.

For each target position, we applied a sequence of dither offsets on a 3 × 3 position grid with grid spacings of 0.″5, resulting in an effective FOV of about 4″ × 4″. Because the faint circumstellar material around IRS5 is rather widespread, we took additional exposures on a 3 × 3 position grid with grid spacings of 2.″0 and 2.″2, increasing the effective FOV to about 7.″4 × 7.″4. In total, we gathered 27 exposures on IRS5, 6 exposures on the position intermediate between IRS5 and UC1, 6 exposures on UC1 and 18 exposures on B273. To allow proper sky subtraction, science exposures (with the AO loop closed, of course) were interleaved every 10 minutes by several (typically 5-6) exposures on the sky position (although void of stars and diffuse emission, with the AO loop open).

Table 1. SINFONI observation parameters

Target	R.A. (J2000)	DEC. (J2000)	Exp. Time (s)	Telluric STD
M17-IRS5	18 20 24.60	−16 11 39.4	27×60	HIP 091126 (G2 V)
	18 20 24.71	−16 11 37.1	6×60	HIP 094378 (B5 V)
M17-UC1	18 20 24.82	−16 11 34.9	6×60	HIP 094378 (B5 V)
M17-B273	18 20 25.07	−16 11 33.9	18×60	HIP 092470 (B2 IV)

To correct for telluric features and to flux-calibrate the science exposures, each night they were immediately followed by observations of a suitable telluric standard star, applying the same strategy (auto-jitter pattern, fixed sky offset) as for the science targets and matching their airmass. The telluric standard stars used in the three observation nights are listed in Table 1.

During all three nights the observing conditions were good, with sky transparency clear (exception: thin cirrus clouds passing through during the night 2008-09-27/28) and telescope guide probe seeing measurements typically in the range $0\farcs6$ – $1\farcs2$. Correspondingly, the achieved strehl ratios were in the range 20 – 40%, as directly measured on the spectrally collapsed data cubes.

Dark frames, lamp flats, and arcs (taken with SINFONI's internal Neon and Argon lamp for the purpose of wavelength calibration) were obtained through the SINFONI scientific calibration plan. All basic steps of data reduction (flat-fielding, sky subtraction, bad pixel and atmospheric distortion correction) as well as the wavelength calibration were performed with the SINFONI data reduction pipeline. Final merging of the fully reduced and wavelength calibrated individual data cubes to one mosaic covering all science targets was performed within the SINFONI pipeline, too.

3.2. Ancillary near- to mid-IR data

The *JHKL* AO imaging was carried out in 2003 June using NAOS/CONICA (NACO; Lenzen et al. 2003; Rousset et al. 2003) on the ESO VLT at the Paranal observatory, Chile. The FOV is $27'' \times 27''$ with pixel resolution of $0\farcs027$. The 3σ limiting magnitudes are $J = 20.2$, $H = 19.7$, $K = 19.3$, and $L = 15.2$. The photometry was carried out merely for the point sources within the FOV of SINFONI data (see Fig. 1). The magnitudes of these point sources were extracted based on a variety of aperture sizes on the purpose of aperture correction. The final magnitudes with aperture correction are calibrated with photometric standard stars, which are HD 110621 for *J*-band ($J = 8.91$), HD 188112 for *HK*-band ($H = 10.78$, $K = 10.89$), and HD 161743 for *L*-band ($L = 7.61$). The astrometry is adjusted by referencing the NACO point sources with the detections of the SINFONI data whose astrometry was calibrated using the 2MASS catalog. With this procedure, the relative astrometric difference between the NACO data and SINFONI data is better than $0\farcs1$.

The TIMMI2 (**T***hermal* **I***nfrared* **M***ultimode* **I***nstrument*; Reimann et al. 1998) mid-IR imaging was carried out in 2003 July at the ESO 3.6 m telescope at La Silla, Chile. The observations covered the *N*1, *N*10.4, and *Q*1 bands with $\lambda_{\rm eff}$ of 8.7 μm, 10.38 μm, and 17.72 μm, respectively, and all had FOV of $55'' \times 38''$ with pixel scale of $0\farcs2$. All data are limited by diffraction with a FWHM (Full Width Half Maximum) of $0\farcs7$.

The M 17 UC1 – IRS5 region was imaged with VISIR (**V***LT* **I***mager and* **S***pectrometer for mid-***I***nf***R***ared*; Lagage et al. 2004) in 2006 May through the Sic filter ($\lambda_{\rm eff} = 11.85\,\mu$m). The observation procedures are described in N+07. The image is of good quality (FWHM $\approx 0\farcs32$) limited by diffraction, with pixel scale of $0\farcs127$. The astrometry of the TIMMI2 and VISIR imaging data were calibrated on the basis of the NACO data. The astrometric accuracy is better than $0\farcs1$ throughout the FOV centered on the M 17 UC1 – IRS5 region.

The spectroscopy of the *N*-band silicate absorption feature was performed with TIMMI2 at the ESO 3.6 m telescope at La Silla, Chile, within the same observation run of UC1 (N+07). The seeing was $0\farcs7$; the slit width was $1\farcs2$.

4. Results

4.1. High angular Resolution Near-IR imaging

The M 17 UC1 – IRS5 region outlines a typical interface between an H II region and a PDR, as characterized by a prominent IF seen in our previous, lower resolution near-IR images (e.g. Hoffmeister et al. 2008, CZ+12). Our high-resolution images unveil many fine structures toward this region which were not revealed before (see Fig. 1). Part of the results had been published for UC1 (N+07). Interestingly, the two luminous infrared objects (M 17 IRS5, M 17 B273) are resolved to have more than one component in the high-resolution near-IR images. If they actually are multiple systems, one needs to review these objects because they were treated as single high-mass YSO candidates, and thus the primary's brightness would have been overestimated.

The *JHKL* magnitudes of the objects inside the white box are listed in Table 2. The brightest component of the IRS5 system is treated as the primary star, namely IRS5A, and followed by four other fainter companions IRS5B, IRS5C, IRS5D, and IRS5E. Similarly, B273A is chosen as the primary star of the binary B273.

4.1.1. Point sources with IR excess

Fig. 2 shows the *HKL* color-color diagram of the objects from Table 2. Objects located to the right of the reddening vectors are suggested to show infrared excess which traces the circumstellar material around YSOs. The level of infrared excess somehow relates to the amount of circumstellar material (Lada & Adams 1992), which in turn reflects the evolutionary stage of YSO. All the objects with accurate *L*-band magnitudes show infrared excess, indicating that they are YSOs. IRS5A, B273A and B273B all show infrared excess resembling to classical T Tauri stars (CTTS). IRS5B seems to have a larger infrared excess, implying a younger evolutionary stage. IRS5C is the reddest source apart from UC1, although its infrared excess is comparable to that of IRS5B. Without proper spectral type classification, we can only establish a crude mass sequence for these point sources according to their dereddened magnitudes. However, it is impossible to extract exact extinction values for these sources solely based on their locations in Fig. 2. The close positions in the *HKL* color-color diagram suggest that all sources except IRS5C have similar reddening. The extinction of IRS5C, however, is

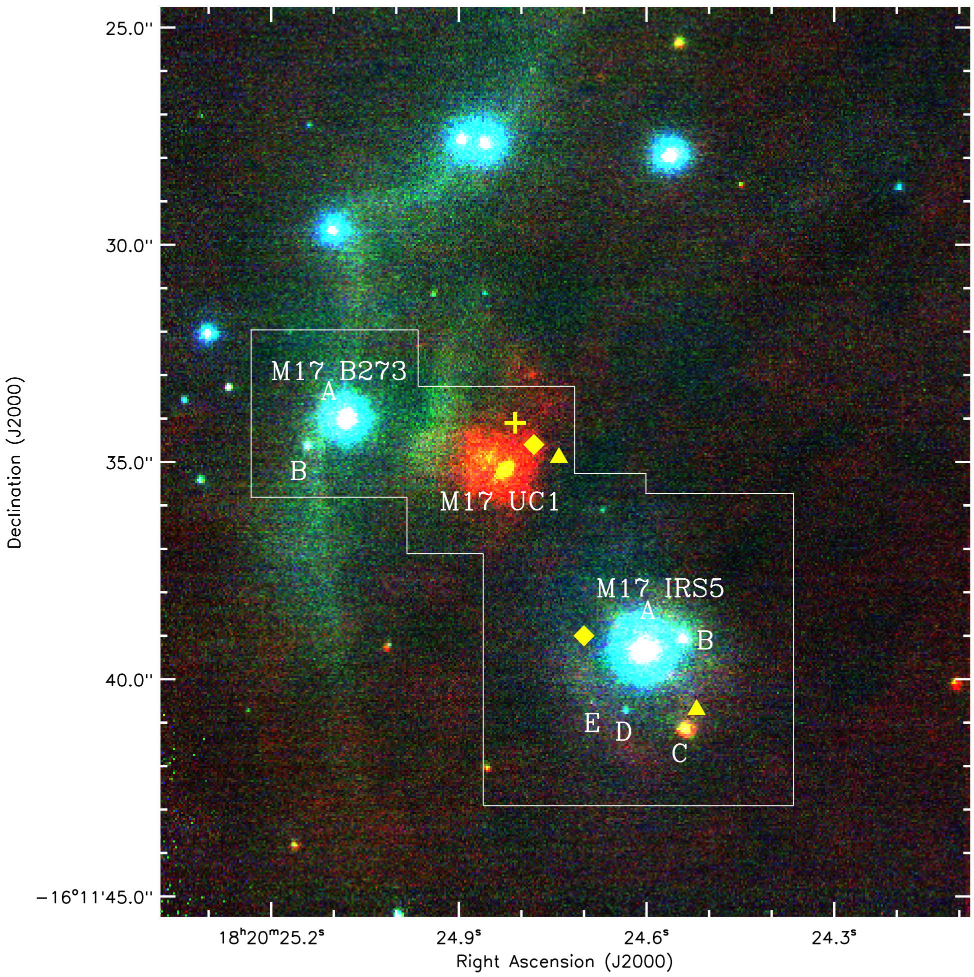

Fig. 1. Three-color image of the M 17 SW PDR taken by NACO at three near-IR broadband filters (blue: *H*; green: *K*; red: *L*), with the area of the SINFONI integral field spectroscopy outlined in the white box. Individual point sources discussed in this paper are labeled. Three types of maser are marked according to their coordinates: 22-GHz water masers (filled triangles, Caswell 1998; Johnson et al. 1998); Class II methanol masers at 6.66 GHz (filled diamonds, Caswell et al. 1995, 2000); OH masers at 1.67 GHz (thick plus, Caswell 1998).

Table 2. NACO *JHKL* photometry of the point sources in M 17 UC1 – IRS5 region

Source ID	R.A. (J2000)	DEC (J2000)	*J* (mag)	*H* (mag)	*K* (mag)	*L* (mag)
M 17 B273						
A	18 20 25.08	−16 11 34.0	14.03 ± 0.01	12.19 ± 0.01	10.71 ± 0.01	8.89 ± 0.01
B	18 20 25.14	−16 11 34.6	20.11 ± 0.33	17.18 ± 0.05	15.26 ± 0.04	13.25 ± 0.09
M 17 UC1	18 20 24.84	−16 11 35.1	–	–	13.61 ± 0.02	6.20 ± 0.03
M 17 IRS5						
A	18 20 24.60	−16 11 39.4	13.34 ± 0.01	11.38 ± 0.02	9.81 ± 0.01	8.16 ± 0.03
B	18 20 24.54	−16 11 39.0	19.07 ± 0.22	15.09 ± 0.02	13.81 ± 0.02	11.56 ± 0.03
C	18 20 24.54	−16 11 41.2	–	19.13 ± 0.13	14.65 ± 0.03	9.69 ± 0.01
D	18 20 24.63	−16 11 40.7	–	17.97 ± 0.12	16.32 ± 0.07	15.27 ± 0.40
E	18 20 24.69	−16 11 40.5	–	19.69 ± 0.32	17.75 ± 0.18	–

Notes. Coordinates of point sources adopted here are a compromise between the astrometry of NACO and SINFONI data, whose differential has been checked less than $0\farcs1$ throughout the FOV.

about three times higher. From the *H*-band magnitudes, we suggest that IRS5A is most massive source, followed by B273A and IRS5C, IRS5E has the lowest mass while the other sources have masses in between.

The area enclosed by the white outline harbors several types of maser, such as water (H_2O) maser at 22 GHz, hydroxyl (OH) maser at 1.665 GHz and Class II methanol maser at 6.66 GHz. Such a variety of maser is commonly found toward regions of massive star formation (e.g. Fontani et al. 2010; Breen et al. 2010). Particularly, the Class II methanol maser is believed to be radiatively pumped, and typically coincides in position with hot molecular cores, UCH II regions, OH masers and near-IR

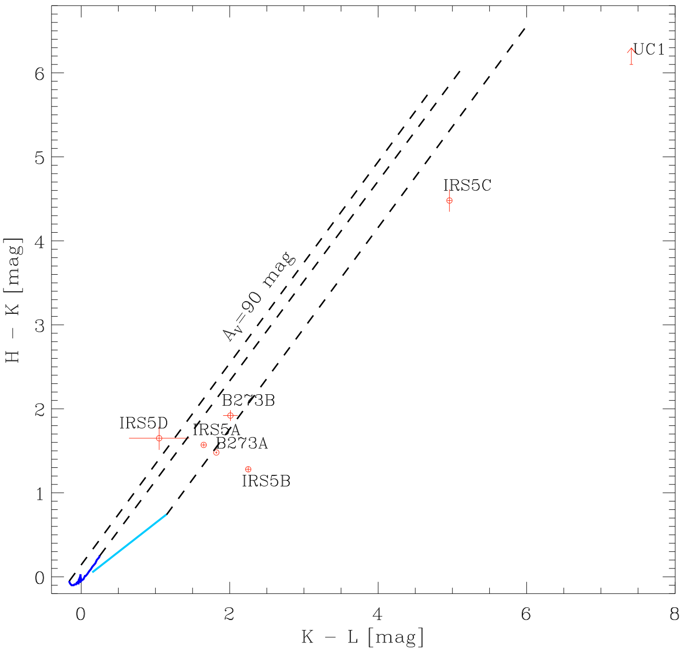

Fig. 2. NACO $K-L$ versus $H-K$ color-color diagram. The blue curve denotes the intrinsic colors of main-sequence stars (Ducati et al. 2001); the cyan line corresponds to the locus of T Tauri stars (Meyer et al. 1997). Reddening vectors (dashed lines) with slope of $E(H-K)/E(K-L) = 1.2$ (Hoffmeister et al. 2008) are drawn. Their lengths equal to visual extinction of 90 mag.

sources (Fontani et al. 2010). Note that H_2O, OH, and 6.66-GHz methanol masers are all detected in the close vicinity of UC1, which coincides with the expectation of a massive forming star. Moreover, a 6.66-GHz methanol maser is detected in close proximity to IRS5A. The H_2O maser at 22 GHz is closer to IRS5C than to IRS5A. If the 22-GHz H_2O maser is associated with IRS5C, it might be a high-mass YSO too. The other possibility is that the 22-GHz H_2O maser is associated with IRS5A, coexisting with the 6.66-GHz methanol maser.

4.1.2. Diffuse emission

A bright rim crossing between the B273 binary is clearly seen in Fig. 1. This rim is a portion of the IF in M 17 seen in larger view (e.g. CZ+12) that represents the boundary between the H II region (to the northeast) and M 17 SW (to the southwest). We note an elongated, bar-like emission feature 2″ west to the IF. This emission bar is nearly parallel to the IF, and shows similar brightness and color with the IF. However, the emission bar has a smooth boundary while the IF is very sharp. Hence, the emission bar might not have the same physical origin as the IF.

The near-IR polarization studies toward M 17 (CZ+12) revealed a bar-like feature enhanced in *K*-band polarized light lying west to the IF. Fig. 3 shows the comparison between *K*-band polarization and NACO/*K* image. The polarization pattern centered on IRS5A had been discussed in CZ+12. The high polarization degree of UC1 is consistent with its two reflection lobes (N+07). At the position of the emission bar seen in NACO/*K* image, a concentration of polarization vectors ~ 10% – 15% marks the location of an IRN. From the pattern of these polarization vectors, UC1 is the best candidate for the illuminating source of the IRN. In fact, the coincidence the two bar-like features seen in different manners indicates a mass concentration of gas and dust associated with UC1 in a bar-like shape.

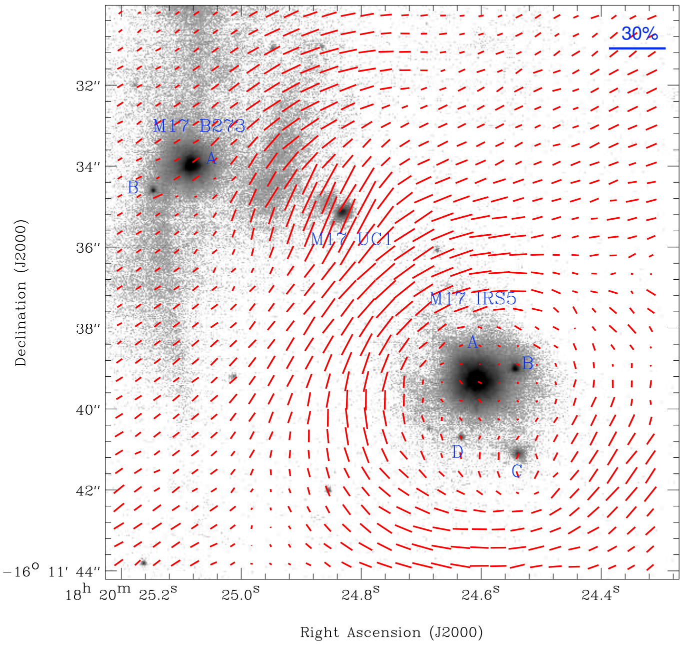

Fig. 3. IRSF/*K* polarization vectors (red lines; CZ+12) overlaid on NACO/*K* image (grey scale).

4.2. Mid-IR imaging

Previous mid-IR imaging showed round morphologies both for UC1 and IRS5 with angular resolution 1 – 2″. Interestingly, the new VISIR image at 11.85 μm with angular resolution ≈ 0″.3 reveals substructures seen in Fig. 4 for both objects. The IF is still visible at this wavelength, but much fainter than in the *K*-band.

UC1 shows an elongated feature toward northwest, which agrees well with its circumstellar disk orientated at P.A. (from north to east) ≈ 146° (shown in yellow dashes in Fig. 4). Moreover, the two parts separated by the circumstellar disk are asymmetric, with the northeastern part more extended. This asymmetric structure can be explained by an inclined circumstellar disk with angle ≈ 30° with respect to the line of sight (hereafter LOS), which is proposed by N+07 to reproduce the *K*-band asymmetric structure which possesses a much brighter southwestern lobe. Besides the mid-IR emission in the close vicinity of UC1, a structure extending to north is more worthy to note. Interestingly, it is spatially coinciding with the IRN discussed in Sect. 4.1.2, and fully covers the area of substantial *K*-band polarization. Conversely, the bar-like feature seen in *K*-band covers only a portion of the IRN.

The high-sensitivity VISIR image shows two lobes separated by a dark lane orientated at P.A. ≈ 30° for IRS5A. Unlike UC1, the *K*-band polarization level is very small in the bulk area of IRS5A. And the *K*-band polarization found in east and south of IRS5A has no mid-IR counterparts; only the mid-IR feature in northeast of IRS5A coincides with *K*-band polarization.

Besides the two bright objects mentioned above, B273A and IRS5C are also visible in the VISIR 11.85 μm image; IRS5C is even brighter than B273A at this wavelength.

In addition, the mid-IR images at other wavelengths taken by TIMMI2 show only the two bright mid-IR objects, UC1 and IRS5A, because of the lower angular resolution and sensitivity. Thus, these mid-IR images taken by TIMMI2 are not shown here, but only the flux densities of UC1 and IRS5A are listed in Table 3.

Table 3. Mid-IR flux densities of the YSOs in the M 17 UC1 – IRS5 region

Object	8.7 μm^a (mJy)	10.38 μm^a (mJy)	11.85 μm (mJy)	17.72 μm^a (mJy)	20.6 μm^c (mJy)
M 17 B273A	-	-	46 ± 22^b	-	-
M 17 UC1	18700 ± 1300	7300 ± 1000	31300 ± 1100^a	146700 ± 29700	128500 ± 6800
M 17 IRS5A	3200 ± 1600	6800 ± 1500	9700 ± 1100^a	130000 ± 31000	103900 ± 5500
M 17 IRS5C	-	-	256 ± 25^b	-	-

Notes. $^{(a)}$ 2.″0 aperture. $^{(b)}$ 0.″4 aperture. $^{(c)}$ 3.″2 aperture from K+02.

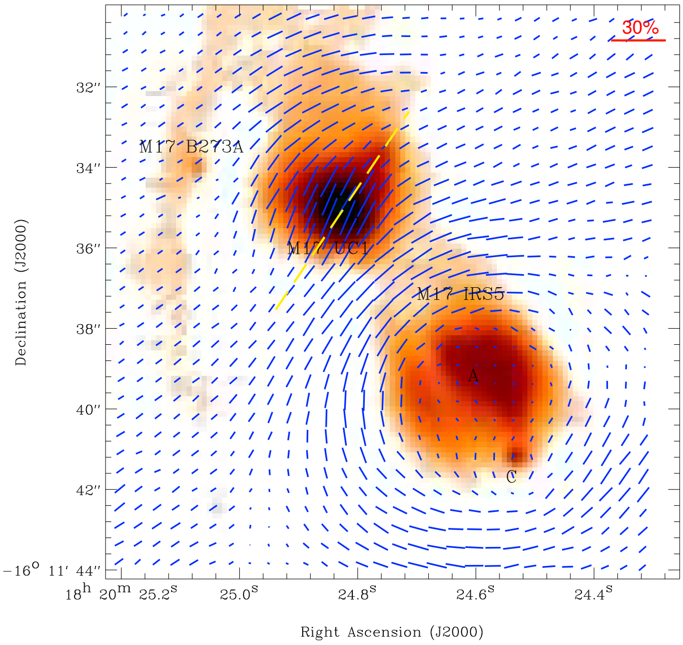

Fig. 4. VISIR 11.85 μm image of the M 17 UC1–IRS5 region. IRSF/*K* polarization vectors (blue lines; CZ+12) are overplotted as well. The disk position angle is denoted by the yellow dashes with P.A of 156° (N+07).

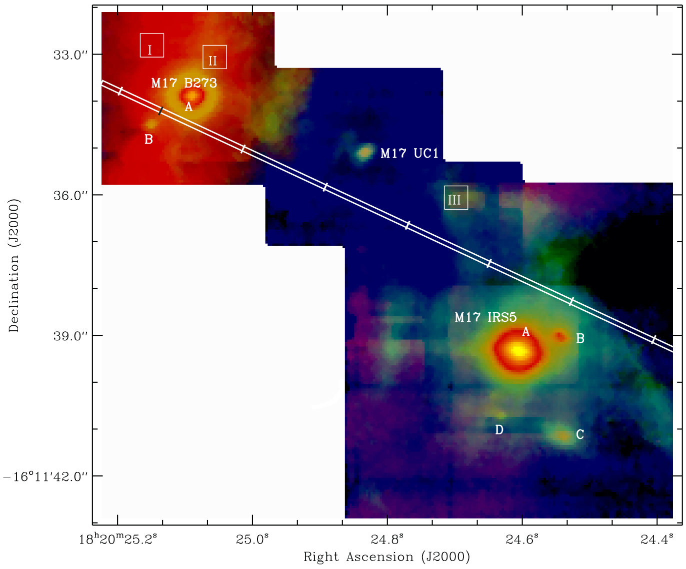

Fig. 5. Three-color image created from the emission (line+continuum) of three near-IR lines (red: Brγ 2.167 μm, green: H_2 1 – 0 S(1) 2.122 μm, blue: He I 2.059 μm). The three squares (I, II, and III) mark selected positions representing H II region, ionization front, and PDR. A strip line with tickmarks is also drawn perpendicular to the IF of M 17 SW. Offset at each tickmark is −1, 0, +2, +4, +6, +8, +10, +12 in arcsec from northeast to southwest, respectively.

4.3. SINFONI near-IR spectroscopy of diffuse content

The SINFONI observations are centered on IRS5, and are extended northeast to cover UC1 and B273. Fig. 5 shows the three-color composite of three lines. This figure reveals both the stellar content and diffuse emission in that area. For each object visible in Fig. 5, a SINFONI $H + K$ spectrum is available. However a spectral classification could only be obtained for IRS5A and B273A (Sect. 4.4), while the S/N of the other spectra was not sufficient. Brγ and 2.059 μm He I 2^1P–2^1S line emission are detected throughout the FOV. The location of the H II region and the IF is traced by the very strong Brγ emission at the top-left corner. On the other hand, the PDR is characterized by 2.122 μm H_2 1–0 S(1) emission. We note H_2 emission surrounding IRS5A and H_2 emission coinciding with the bar-like IRN illuminated by UC1.

4.3.1. Nebular emission lines

The spectra in the three selected regions are shown in Fig. 6, and the observed lines are listed in Table 4. The hydrogen recombination lines such as Brackett series and Paα are visible in all regions. Besides the prominent atomic hydrogen lines, five atomic helium lines are also observed; among them 2.059 μm He I is the strongest one. Molecular hydrogen emission lines longward 2 μm are also observed in region II and III. An emission feature at 2.287 μm is generally classified as H_2 $v = 3 - 2$ S(2) line or unidentified (UID) line (e.g. Lumsden et al. 2001). However, the H_2/UID line might have been mismatched for the H_2 $v = 3 - 2$ S(2) line, because H_2 emission is not spatially coincident with this H_2/UID line in planetary nebulae (e.g. NGC 7027, Okumura et al. 2004). The most potential carrier of this UID line is [Se IV] at 2.287 μm, which is typically detected in highly excited ISM such as planetary nebulae and UCH II regions with hot O-type stars (Blum & McGregor 2008, and references therein). The ionizing sources (O4 binary) of M 17 H II region are very likely to produce the 2.287 μm Se IV line in M 17 SW. The 2.287 μm UID line keeps roughly the same strength throughout the FOV of Fig. 5, indicating that this line traces the ionized gas region. Therefore, we attribute the 2.287 μm line to [Se IV].

4.3.2. H I/H_2 transition zone of M 17 SW

The coexistence of Brγ and H_2 1 − 0 S(1) in region II and III implies that region II and III maybe part of the H I/H_2 transition zone of M 17 SW. In order to investigate the scale size of this H I/H_2 transition zone, Fig. 7 shows line strength variations of

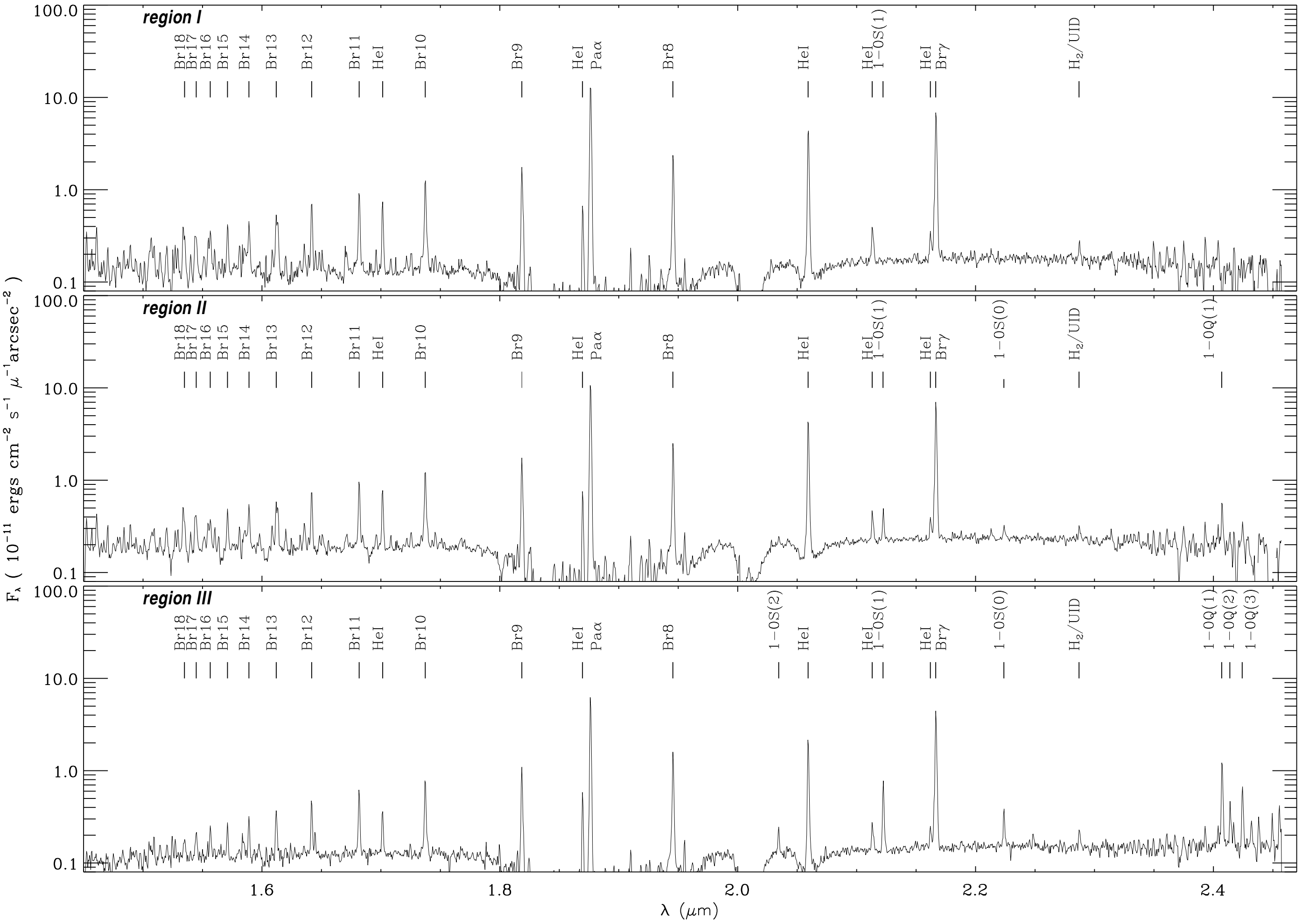

Fig. 6. Ambient spectra of the three selected positions marked by squares in Fig. 5. The telluric feature in the range 1.8 – 2.1 μm is not corrected, because its strength is in proportion to the nebular continuum, which is much weaker than the emission lines. Thus the near-IR emission lines are little affected by the telluric feature.

Brγ, 2.059 μm He I and H_2 1 – 0 S(1) along the strip line denoted in Fig. 5. Peaks of Brγ and 2.059 μm He I both occur around IF. Specifically, the 2.059 μm He I peak occurs ∼ $0\farcs1$ closer to the H II region than the Brγ peak, which defines the IF. Molecular hydrogen starts to appear at offset ∼ $+0\farcs4$, closer to the PDR. Along the strip line, the line strengths of Brγ and 2.059 μm He I show almost identical variations, which both experience fast growth until the IF, rapid drop (offset < $+0\farcs5$), shallow decline (offset between $+0\farcs5 - +2''$), and roughly constant baseline (offset longwards $+2''$). The H_2 1 − 0 S(1) line strength has another type of variation, which shows four peaks along the strip line. The coexistence of atomic gas (H I, He I) and molecular gas (H_2) in the range $+0.4'' - +11.7''$ and the trend further into the PDR indicates that the H I/H_2 transition zone of M 17 SW almost starts from the IF and extends toward the cloud core with a projected scale size more than $12''$ (0.12 pc). However, one has to be cautious because the emission from the HII region and the PDR may partly overlap along the LOS if the configuration is not strictly seen edge-on; the H II region emission lines originate from the surface of the PDR, while PDR emission lines form inside the PDR. In such a case, the co-existence of emission lines like in Fig. 7 will not tell us the true story about H I/H_2 transition zone. Comparison with a strictly edge-on PDR will help to clarify whether this scale size of H I/H_2 transition zone in M 17 SW is reliable or not.

The Orion Bar is a dense PDR like M 17 SW, but nearly edge-on (Allers et al. 2005, and references therein). We measured the scale size of H I/H_2 transition zone in the Orion Bar according to Fig. 3 of Hayashi et al. (1985) to be around $20''$, which is consistent with the distributions of H_2 rotational lines (Allers et al. 2005). Due to the edge-on configuration of the Orion Bar, the scale size measured above is identical to the real scale zie of the H I/H_2 transition zone, i.e. 0.044 pc at the distance of Orion (450 pc; Hoogerwerf et al. 2000). However, the H I/H_2 transition zone in M 17 SW is at least three times Orion Bar in size, which can not be simply explained by the differential properties between the two PDRs. We speculate that the presence of the three emission lines in Fig. 7 is simply a result of geometric projection. Unlike the Orion Bar, M 17 SW is indeed inclined from the LOS with a substantial angle. This result confirms the conclusion of a recent study about the LOS structure of M 17 SW based on H_2 rotational emission (Sheffer & Wolfire 2013).

4.3.3. H_2 excitation

As seen in Table 4, six H_2 emission lines are detected. The two most prominent H_2 lines are H_2 1 − 0 Q(1) at 2.407 μm and H_2 1 − 0 S(1) at 2.122 μm. H_2 emission lines in PDR are generally thought to have two physical mechanisms – fluorescent

Table 4. Observed near-IR lines toward the M 17 UC1 – IRS5 region

λ (μm)	IDs	Transition	Eupper (K)[a]	$F \pm \delta F$(10^{-15} erg cm^{-2} s^{-1} arcsec^{-2})		
Obs.				region I	region II	region III
1.5349	H I	18–4		4.3 ± 2.0	4.9 ± 2.1	1.1 ± 0.4
1.5447	H I	17–4		4.2 ± 1.5	4.8 ± 1.6	1.7 ± 0.3
1.5566	H I	16–4		3.7 ± 1.2	2.6 ± 1.0	1.8 ± 0.6
1.5710	H I	15–4		3.3 ± 1.1	4.9 ± 2.2	2.1 ± 0.2
1.5891	H I	14–4		5.4 ± 0.6	5.7 ± 0.7	2.1 ± 0.6
1.6120	H I	13–4		8.4 ± 1.9	7.6 ± 2.6	3.9 ± 1.2
1.6417	H I	12–4		6.8 ± 2.1	5.6 ± 2.6	4.5 ± 0.4
1.6817	H I	11–4		11.6 ± 0.8	11.4 ± 0.5	7.0 ± 0.5
1.7013	He I	4^3D–3^3P		7.3 ± 1.6	7.4 ± 1.6	3.3 ± 0.3
1.7372	H I	10–4		17.6 ± 1.1	16.8 ± 1.0	9.9 ± 0.6
1.8185	H I	9–4		23.3 ± 1.3	21.8 ± 1.8	13.0 ± 1.3
1.8696	He I	4^3F–3^3D		7.9 ± 0.9	7.8 ± 0.8	5.7 ± 0.7
1.8762	H I	4–3		183.9 ± 1.0	147.8 ± 1.1	74.8 ± 0.7
1.9457	H I	8–4		31.7 ± 1.0	32.1 ± 1.5	19.5 ± 0.8
2.0344	H_2	v =1–0 S(2)	7584	–	0.6 ± 0.4	1.8 ± 0.4
2.0592	He I	2^1P–2^1S		61.2 ± 0.6	60.8 ± 0.6	28.4 ± 0.3
2.1132	He I	$4^{1,3}$–$3^{1,3}$P		4.2 ± 0.8	4.0 ± 0.3	2.4 ± 0.4
2.1224	H_2	v =1–0 S(1)	6956	–	3.3 ± 0.4	8.5 ± 0.2
2.1620	He I	7^3F–4^3D		3.1 ± 0.4	3.0 ± 0.5	1.5 ± 0.4
2.1667	H I	7–4		99.4 ± 0.7	92.8 ± 0.4	57.3 ± 0.3
2.2239	H_2	v =1–0 S(0)	6471	0.0 ± 0.7	1.5 ± 0.5	3.2 ± 0.6
2.2873	[Se IV]	$^2P_{3/2}$–$^2P_{1/2}$		1.2 ± 0.4	1.4 ± 0.4	1.5 ± 0.5
2.4073	H_2	v =1–0 Q(1)	6149	–	7.2 ± 1.0	15.7 ± 0.5
2.4141	H_2	v =1–0 Q(2)	6471	–	–	4.8 ± 0.4
2.4244	H_2	v =1–0 Q(3)	6956	–	4.1 ± 1.2	6.8 ± 0.7

Notes. Lines detected in the averaged spectra of three selected regions. The flux of each line is averaged over each region.
(a) Excitation energy adopted from Dabrowski (1984).

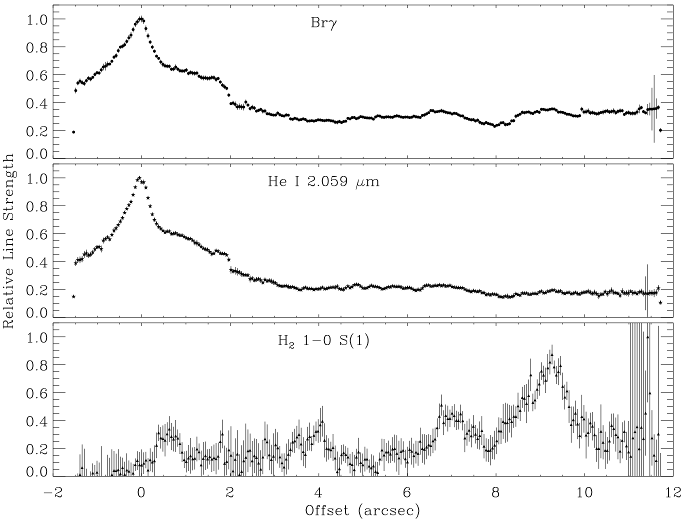

Fig. 7. Line intensity variations of three representative lines – Brγ, 2.059 μm He I, and H_2 1 − 0 S(1) – along the strip line which is perpendicular to the IF of M 17 SW (outlined in Fig. 5). The zero-point is defined at 18: 20: 25.136, −16: 11: 34.21 (J2000), at the maximum strength of the IF; negative offsets point toward the H II region, while positive offsets point toward the PDR.

excitation by FUV photons and thermal excitation in shock fronts. Practically, near-IR H_2 fluorescent spectra have been observed for a variety of classical PDRs such as associated with NGC 2023, Orion Bar, and the northern bar in M 17 (Gatley et al. 1987; Hayashi et al. 1985; Tanaka et al. 1989). Meanwhile, a variety of H_2 spectra have been found to be produced in the shock fronts associated with the jets/outflows found in PDRs (e.g. Nürnberger et al. 2007; Martín-Hernández et al. 2008; Bik et al. 2010). Although these two mechanisms both act occasionally for H_2 emission found in PDRs, they can be distinguished since the corresponding H_2 line ratios are different.

A common way of characterizing the H_2 emission is to evaluate the gas temperature in the framework of a ro-vibrational diagram, which is a plot of the observed column density against the energy of the upper level. The column density, N_j, of the upper level of a given transition can be calculated from the measured line intensity, I, of the corresponding H_2 line via the following formula:

$$N_j = \frac{4\pi\lambda_j I}{A_j h c},$$

where λ_j (the rest wavelength) and A_j (the Einstein A-coefficient) are taken from Turner et al. (1977). If collisional de-excitation plays dominant role, the H_2 molecule will be in LTE and the energy level obeys the Boltzmann distribution. In such distribution, the relative column densities of any two excitation levels can be expressed in terms of excitation temperature $T_{\rm ex}$:

$$\frac{N_i}{N_j} = \frac{g_i}{g_j}\exp\left[\frac{-(E_i - E_j)}{k T_{\rm ex}}\right],$$

where g_j is the degeneracy, E_j is the excitation energy taken from Dabrowski (1984), and k is the Boltzmann constant. If the gas is thermalized at a single temperature, the plot of the logarithm of N_j to g_j ratio against the level energy will reveal a

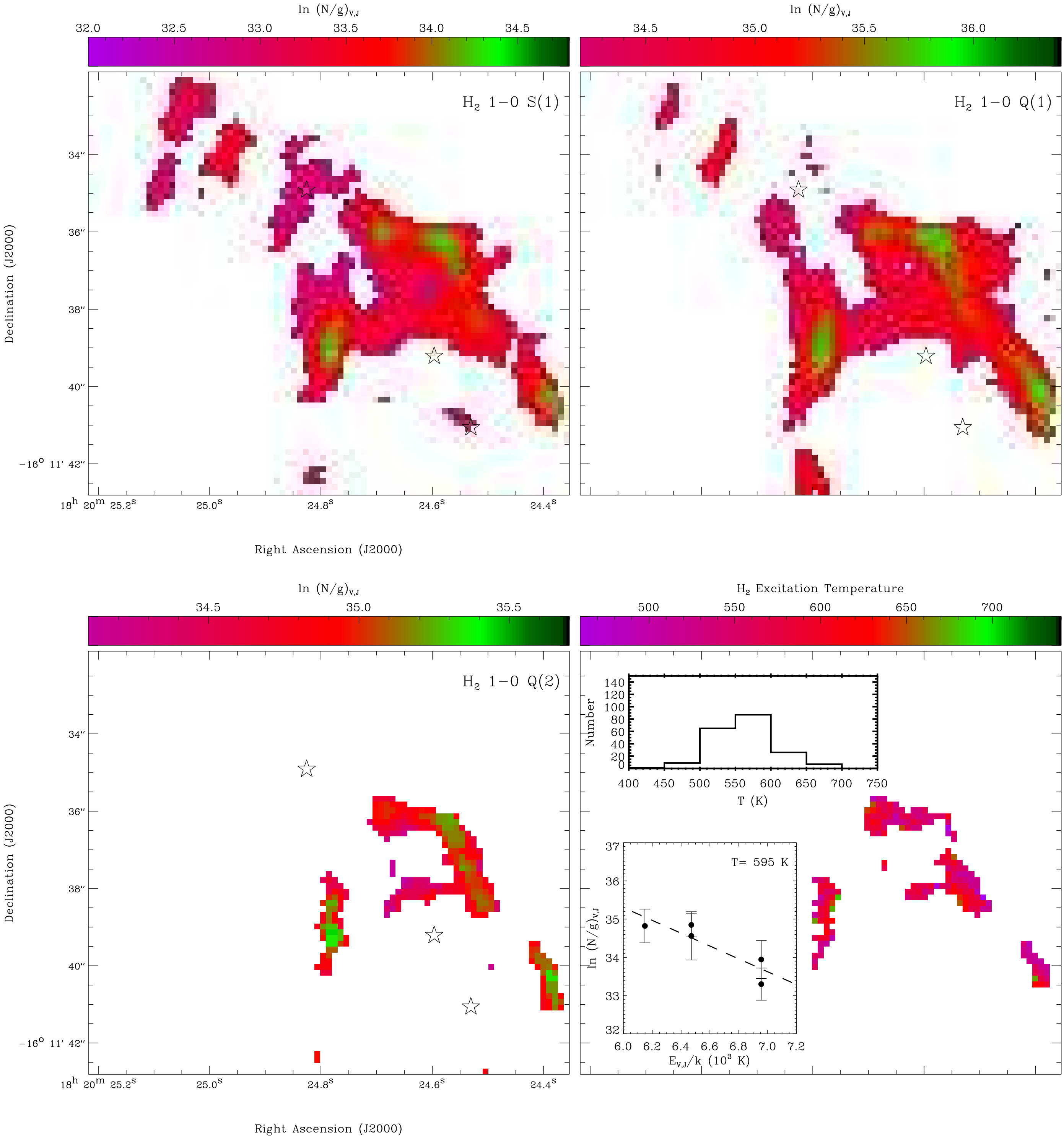

Fig. 8. Column densities of H_2 1−0 S(1), 1−0 Q(1) and 1−0 Q(2) (quadrants I to III) as well as the H_2 excitation temperature map (quadrant IV). In quadrants I to III, IRS5A,C and UC1's positions are marked by asterisks. In quadrant IV, the ro-vibrational diagram based on the H_2 lines (H_2 1−0 S(1), 1−0 S(0), 1−0 Q(1), 1−0 Q(2), and 1−0 Q(3)) averaged over all collected pixels is plotted, as well as the histogram density of H_2 excitation temperature.

straight line, whose slope provides the reciprocal of the excitation temperature.

We implied this method to evaluate the excitation temperature for the detected H_2 emission lines, assuming the same dust attenuation for all lines. Fig. 8 shows the extinction-uncorrected column densities of H_2 1−0 S(1), H_2 1−0 Q(1), and H_2 1−0 Q(2). We excluded the H_2 1−0 S(2) line in plotting the ro-vibrational diagram, because this line is too weak to be significantly detected in most FOV. Except H_2 1−0 S(1) and 1−0 Q(1), the remaining three H_2 lines are weak, although stronger than 1−0 S(2). To increase the S/N ratios for these weak H_2 lines, we degraded the angular resolution of the SINFONI data by rebinning the data with 3×3 array. The resulting S/N ratios are increased by a factor of ~ 3. Note that rebinning is applied merely when the H_2 emission lines are analyzed. Thus, only Fig. 8 and Fig. 10 are plotted in the rebinned pixel scale. For H_2 1−0 S(1) and 1−0 Q(1), a threshold of $S/N \geqslant 3$ is used; for the remaining three H_2 lines, $S/N \geqslant 2$ is applied. The lower-right panel in Fig. 8 presents the map of $T_{\rm ex}$ for H_2 emission, and the histogram of excitation temperatures, as well as the ro-vibrational diagram based on the column densities averaged throughout the collected pixels. The ro-vibrational diagram shows that all five H_2 lines lie along a straight line whose slope corresponds to an excitation temperature ≈ 600 K. We note that the determined $T_{\rm K}$ for each rebinned pixel might have large errors because the adopted H_2 lines just cover a very narrow range of excitation temperature (6100 – 7000 K). Nevertheless, the statistical $T_{\rm ex}$ of the H_2 gas is more meaningful than a specific value for each rebinned pxiel. With the histogram of $T_{\rm ex}$ for all rebinned pixels, we found a peak around 575 K. A single excitation temperature for the H_2 emission indicates that the energy levels are thermally excited. Other discriminators for the two excitation mechanisms of H_2 emission such as H_2 1−0 S(1)/2−1 S(1) ratio and H_2 ortho-to-para ratio both indicate thermal excitation.

For fluorescence emission, each vibrational level has N_j/g_j lying along a separate "branch", and the rotational population within each level can be approximated by a thermal distribution. If there are transitions from several levels, a curved line in the ro-vibrational diagram would therefore provide evidence for non-LTE process (Martín-Hernández et al. 2008). The H_2 lines at higher levels, e.g. $v = 3-2$, can be useful to distinguish between the two mechanisms. In the case of the M 17 UC1 – IRS5 region, the merely available $v = 1 - 0$ transitions cannot be used to discriminate between shock and fluorescent excitation, because they will lie along a straight line in the ro-vibrational diagram for both mechanisms if uncertainties are considered. Moreover, in dense PDRs the lower H_2 levels will be thermalized as like in shock fronts. This degeneracy between dense PDRs and shock fronts prevents us to exactly characterize the H_2 emission from the ro-vibrational diagram. This approach is more meaningful for the regions with moderate/strong H_2 emission at all transitions. Indeed, it is curious to know whether weak H_2 emission area possessing the same excitation mechanism with the stronger H_2 emission area.

In an H ii region, another attempt to qualitatively characterize the H_2 emission comes from the comparison of molecular and atomic hydrogen emission. The molecular-to-atomic line ratio, particularly the ratio H_2 1−0 S(1)/Brγ, is $\leqslant 1$ in active galaxies (starburst, Seyfert, and ultra-luminous infrared galaxies) and star-forming regions (Hatch et al. 2005, and reference therein). Conversely, this ratio is $\geqslant 1$ in outflow regions (Hatch et al. 2005; Martín-Hernández et al. 2008). All regions showing H_2 1−0 S(1) emission yield H_2 1−0 S(1)/Br$\gamma \ll 1$. The extremely strong hydrogen atomic emission observed here indicates very intense incident stellar radiation field, which makes the FUV pumping as the most likely excitation mechanism for the molecular hydrogen emission observed in our study. Further indirect evidence also points out that FUV fluorescence is the most plausible excitation mechanism. For instance, H_2 1−0 S(1) and H_2 1−0 Q(1) emission seen in the top two panels in Fig. 8 shows some filament structures parallel to the IF. This H_2 emission can not be characterized by the aforementioned approaches, since just emission of 1−0 S(1) and 1−0 Q(1) are available. One may argue, however, that the H_2 emission lying parallel to IF can be produced in shock waves driven by the IF. An identical case is the Orion Bar PDR which shows H_2 emission behind itself with a ratio of H_2 1−0 S(1)/2−1 S(1) ∼ 3 resembling shock excitation (Hayashi et al. 1985). Nevertheless, Burton et al. (1990) proposed a high-density PDR model to explain the observed line ratio because the typical shock speed, $\leqslant 3\,{\rm km\,s^{-1}}$, of an expanding H ii region driving into molecular gas is too low to significantly excite low-v H_2 transitions. Considering the common properties between M 17 SW and Orion Bar, we tend to neglect shock excitation for the IF-parallel H_2 emission. Complementally, in Fig. 9 the IRN illuminated by IRS5A and by UC1 (the one discussed in Sect. 4.1.2) spatially coincides with H_2 emission. H_2 fluorescent emission has been found for some large-scale IRN associated with star-forming regions such as NGC 2023 and Orion Bar (Gatley et al. 1987; Burton et al. 1990). Although the IRN here are associated with luminous IR stars, we speculate that this coincidence is an indirect evidence in favor of FUV fluorescence excitation.

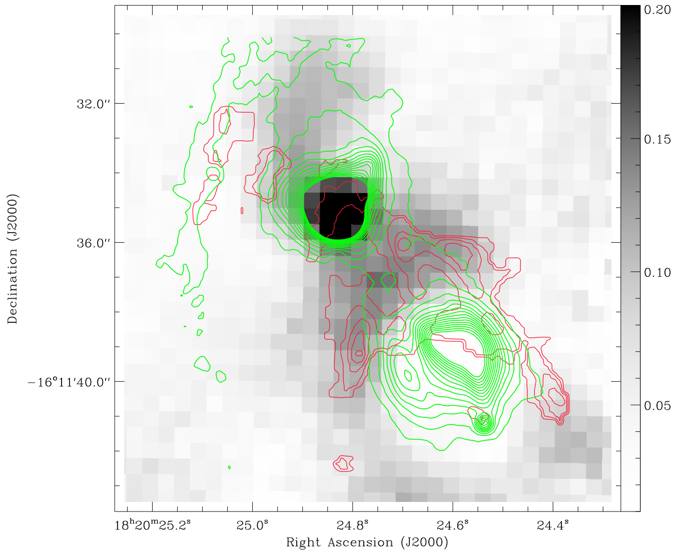

Fig. 9. H_2 1−0 S(1) line flux (red contours) overlaid on the IRSF/*K* polarization degree image (grey scale; CZ+12). H_2 1−0 S(1) contour levels start from $2\times10^{-15}\,{\rm erg\,cm^{-2}\,s^{-1}\,arcsec^{-2}}$ with four intervals, each of $2\times10^{-15}\,{\rm erg\,cm^{-2}\,s^{-1}\,arcsec^{-2}}$. Green contours correspond to the VISIR 11.85 μm emission.

In Fig. 10 we show the H_2 1−0 Q(1)/1−0 S(1) ratio map, which covers most of the H_2 emitting regions. The H_2 1−0 Q(1)/1−0 S(1) ratio intrinsically varies with the physical conditions of H_2 gas. Luhman et al. (1998) modeled H_2 line ratios detected in Orion Bar and Orion S including H_2 1−0 Q(1)/1−0 S(1) ratio for several set of PDR models and thermal excitation by shock front as well. From their modeling, we find distinct H_2 1−0 Q(1)/1−0 S(1) ratios between PDR models and shocked thermal excitation (see Table 1 in Luhman et al. 1998). The H_2 1−0 Q(1)/1−0 S(1) ratios of the H_2 emission in M 17 SW are mostly in the range 1.0 − 3.0. The bulk of the H_2 emission regions have a H_2 1−0 Q(1)/1−0 S(1) ratio ∼ 1.8, which is between the ratios of two PDR models of $n_{\rm H} = 10^6\,{\rm cm^{-3}}$, $G_0 = 10^4$, $T_0 = 500$ K, and $n_{\rm H} = 10^6\,{\rm cm^{-3}}$, $G_0 = 10^5$, $T_0 = 1000$ K, respectively. In contrast, the H_2 1−0 Q(1)/1−0 S(1) ratio predicted by the shocked thermal model is 0.7, much lower than the ratios observed here. The extinction-corrected H_2 1−0 Q(1)/1−0 S(1) ratio will be smaller than the observed one, however, the decrease caused by dereddenning is not big enough to lower this ratio to a thermal value.

We note quite uniform distributions of line ratios such as H_2 1−0 S(1)/2−1 S(1), H_2 1−0 S(1)/Brγ, and H_2 1−0 Q(1)/1−0 S(1) across all H_2 emitting areas in the M 17 UC1 – IRS5 region, which indicates a uniform mechanism for the entire H_2 emis-

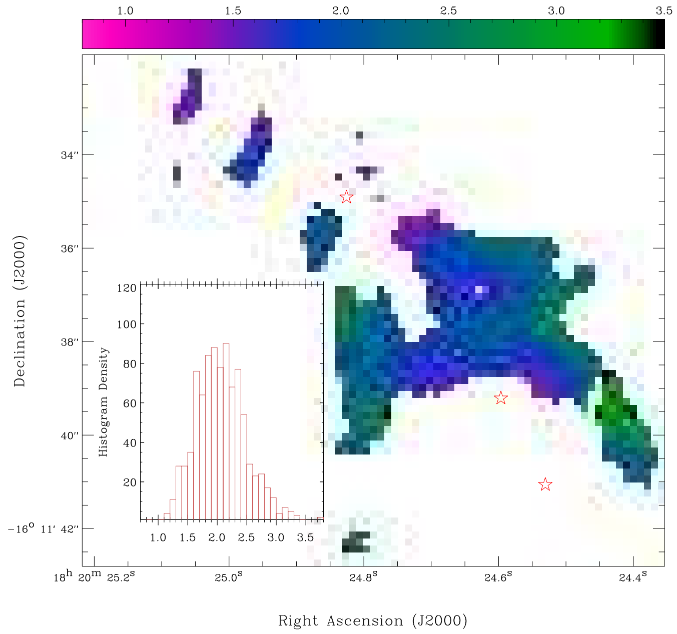

Fig. 10. Map of H_2 1−0 Q(1)/1−0 S(1) ratio, and corresponding histogram density at lower left corner. The three asterisks are as same as in Fig. 8.

sion. All the above properties of H_2 emission can be well explained in the scenario that the H_2 molecules inside M 17 SW are initially pumped to vibrational states by FUV fluorescence, and then are deexcitated from high-v levels to low-v levels due to the high-frequency collision inside the high-density PDR. Due to this process, H_2 emission is mostly in the form of low-v vibrational states and pure rotational states. Besides the $v = 1 - 0$ H_2 emission lines reported here, Sheffer & Wolfire (2013) reported mid-IR pure-rotation H_2 emission at $v = 0 - 0$ states toward M 17 SW.

4.4. SINFONI near-IR spectroscopy of point sources

The SINFONI H+K spectra of the YSOs in M 17 UC1 – IRS5 region, are crucial to understand their fundamental properties such as effective temperature and luminosity class via analyzing the characteristic spectral features (see Fig. 11). Objects located inside an HII region or a PDR require special care due to the contamination by nebular emission. The nebular contamination is evaluated in an annulus closely encircling the stellar contours. The spectra of IRS 5A and B273A have sufficient S/N to maintain a reliable classification, while the other sources are too faint.

The most prominent lines in Fig. 11 are the hydrogen Brackett absorption lines seen in IRS5A, the CO 2−0 bandhead absorption for B273A, and the H I Paα and Brγ emission for UC1. The H I emission lines of UC1 are reminiscent of the common emission features of YSOs, which are due to the accretion flows falling onto the YSOs. However, we note from Fig. 5 that the emission lines mostly form in the two reflection lobes of UC1, and very little part directly comes from UC1 which is mostly obscured by its edge-on disk. The H I emission lines seen in UC1's spectrum arise most likely in the associated HCHII region. The shape of H I emission region oriented perpendicularly to the edge-on circumstellar disk of UC1, is suggested to trace the relevant HCHII region expanding preferentially along the polar direction because of the lower-density gas in polar regions.

The normalized spectra of IRS 5A and 273A are shown in Fig. 12 and 13, respectively. IRS5A's spectrum displays strong hydrogen Brackett absorption lines. The sole characteristic line in the K-band, Brγ, indicates a temperature class later than B3, since its effective temperature is not high enough for the growth of 2.113 μm He I line which appears for early-B stars (Hanson et al. 1996). The Brγ equivalent width (EW) is quantified to disentangle the ambiguity between mid-B (kB4–B7) and late-B/early-A (kB8–A3); the latter shows Brγ EW greater than 8 Å while the former shows Brγ EW between 4 Å and 8 Å (Hanson et al. 1996). The Brγ EW of IRS5A is measured to be 4.8 Å, constraining its temperature class to be kB4–B7. How does the K-band temperature class link to the optical spectral class? In the study by Hanson et al. (1996), six reference stars with known optical spectral type are assigned to a K-band spectral type of kB4–B7. Four out of the six stars have optical spectral classes of B3–B6, with three dwarfs and one giant. The remaining two are optically classified late-B/early-A supergiants. Hanson et al. (1996) stressed that the spectral types solely based on K-band spectrum are not sensitive to surface gravity and show ambiguity between mid-B stars and late-B/early-A supergiants.

The H-band spectrum provides more spectral type indicators. The presence of strong Br11 line and weak 1.701 μm He I line (EW < 0.2 Å) both point out a spectral class later than early-B (Hanson et al. 1998). Moreover, the Br11 EW of IRS5A is determined as 4.1 Å, suggesting mid-B spectral class. With the known spectral type range of IRS5A, it is possible to distinguish dwarfs and supergiants based on the Br11/1.701 μm He I ratio. Hanson et al. (1998) found for early/mid-B stars that this ratio is consistently larger for dwarfs than for supergiants of the same spectral class; e.g. this ratio is about 3.0 in average for B4–B7 supergiants. In the case of IRS5A, the large ratio of Br11 to 1.701 μm He I ($\gtrsim 20$) indicates a luminosity class close to dwarf.

Some He I lines (e.g. 1.701 μm, 2.113 μm) are crucial diagnostic lines to separate early-B stars from later type stars (e.g. Hanson et al. 2005; Bik et al. 2005). Moreover, the difficulty in distinguishing dwarfs and giants solely based on near-IR spectral features also prevent us to better constrain the luminosity class of IRS5A. According to the $H + K$ spectral characteristics, we suggest a spectral type of B3–B7 V/III for IRS5A.

B273A's H-band spectrum does not show any significant characteristic line. Its K-band spectrum only shows 2.3 μm CO $2 - 0$ bandhead absorption. The CO bandhead absorption longwards of 2.29 μm is typical of late-type stars (e.g. Wallace & Hinkle 1997), whose outer atmospheric layers have the proper temperatures ($\sim 1000 - 3000$ K) to produce such features. Moreover, low-mass Class II/III YSOs (temperatures identical to those of late-type stars) might also show CO bandhead in absorption despite of the circumstellar material because the circumstellar veiling is less than that of Class I YSOs and consequently overwhelmed by the photospheric feature (Casali & Eiroa 1996).

The CO bandhead absorption is found to be tightly related with the effective temperature and luminosity class for giants and supergiants. The EW of CO bandhead increases linearly with temperature declining for giants and supergiants, respectively, and the later has higher EW than the former of the same effective temperature (e.g. González-Fernández & Negueruela 2012). The CO bandhead of B273A coincides in depth and width with that of the reference star, a G4 giant (see Fig. 13). Indeed, a supergiant needs to have earlier temperature class to match the EW of a giant's CO bandhead. We measured the EW of CO

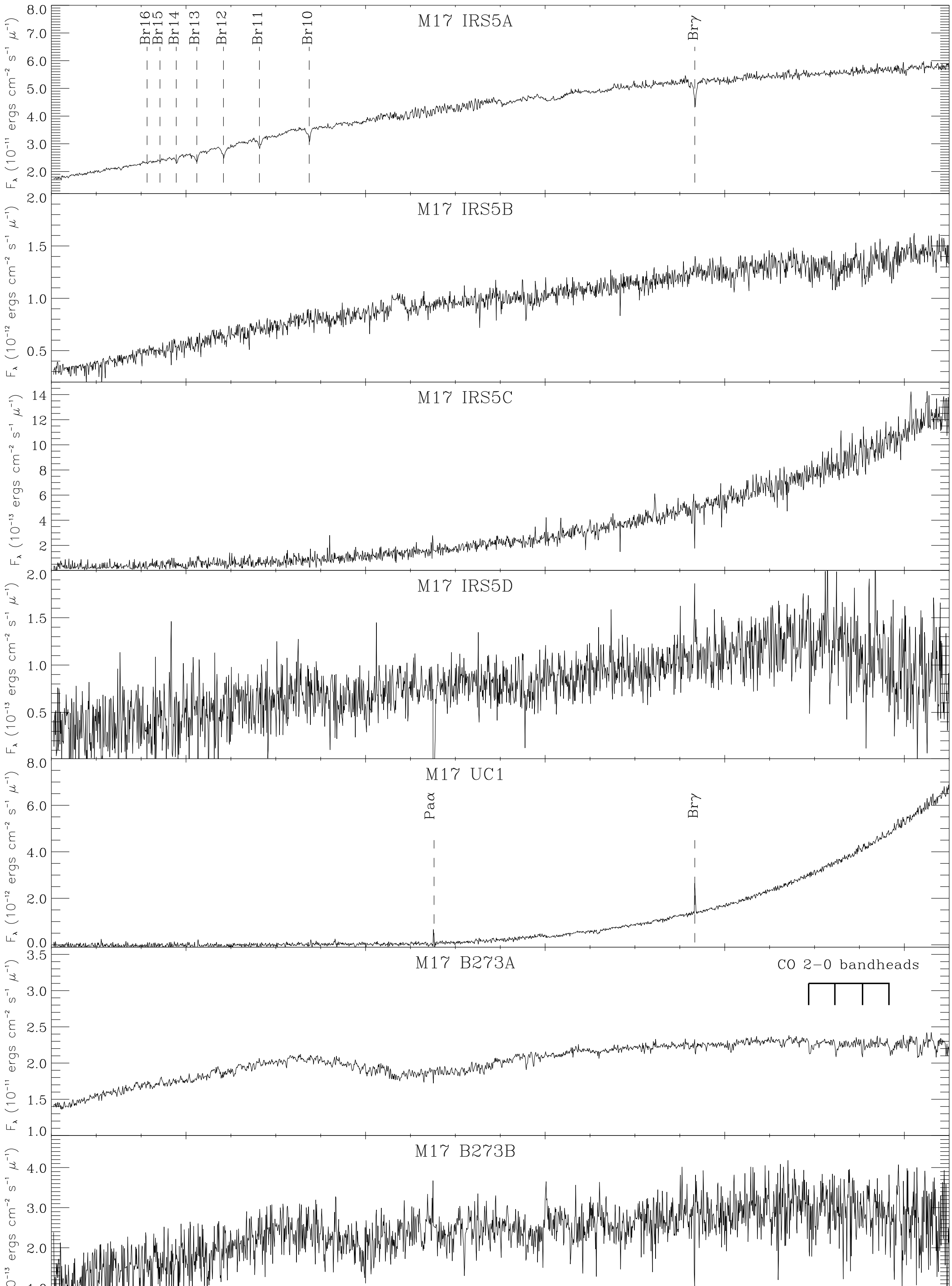

Fig. 11. Flux-calibrated SINFONI $H + K$ spectra of the point sources in M 17 UC1–IRS5 region. All natural spectral features are marked, e.g. H I emission/absorption lines and CO $2-0$ bandheads in absorption.

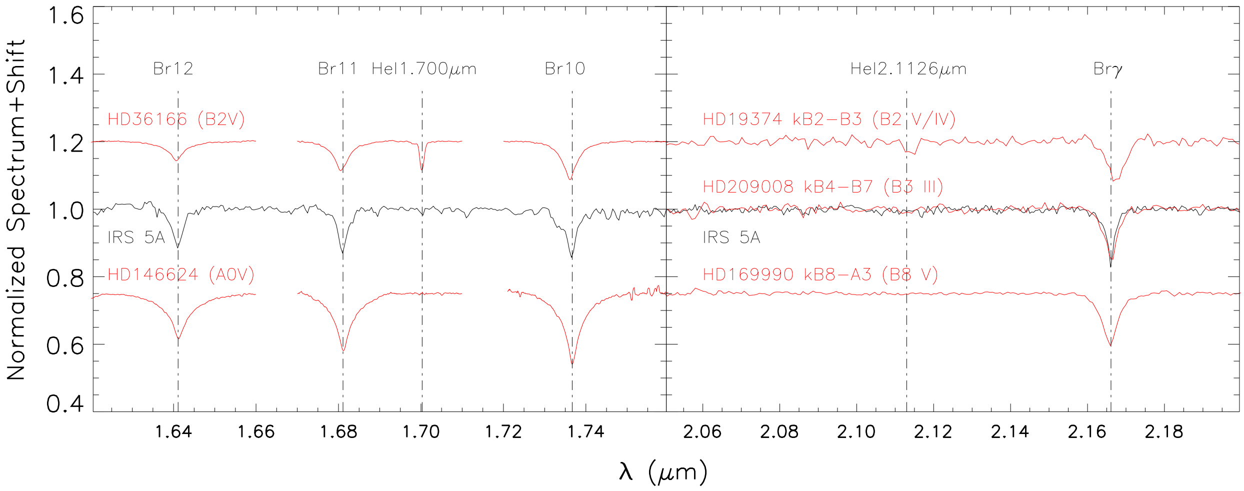

Fig. 12. Normalized SINFONI $H + K$ spectrum of IRS5A (black curve). For comparison, the spectra of several reference stars are displayed; they are adopted from the literature as follows: B2 V (HD 36166), A0 V (HD 146624) from Hanson et al. (2005); B2 V/IV (HD 19374), B3 III (HD 209008), B8 V (HD 169990) from Hanson et al. (1996). All reference spectra are converted to a resolution identical to SINFONI's resolving power.

bandhead for B273A to be ≈ 3.5 Å, which suggesting a spectral type of G4/G5 for a giant and G2/G3 for a supergiant when following Fig. 2 in González-Fernández & Negueruela (2012). Alternatively we checked the EW of CO bandhead for the main sequence stars catalogued by Wallace & Hinkle (1997) and found that B273A's CO bandhead strength is between that of a G8 V (HR 4496) and a K2 V (HR 1084) star. We could not further constrain the spectral type of B273A without other characteristic lines at shorter wavelengths.

A fit example is CEN 34, a mid-G supergiant located along the LOS toward M 17, is classified to be background with respect to M 17 with age between 50–100 Myr (Chen et al. 2013). Upon the consideration of B273A's apparent brightness at short wavelengths, the object should not be in the foreground of M 17. Thus we can rule out the possibility of an early-K dwarf which is only visible at shorter distance. On the other hand, the solution of early-G supergiant puts B273A in the backside of M 17. However, the large amount of molecular gas along the LOS toward the M 17 UC1 – IRS5 region can almost obscure any background object. Therefore, we keep the solution of mid-G giant as the spectral type of B273A.

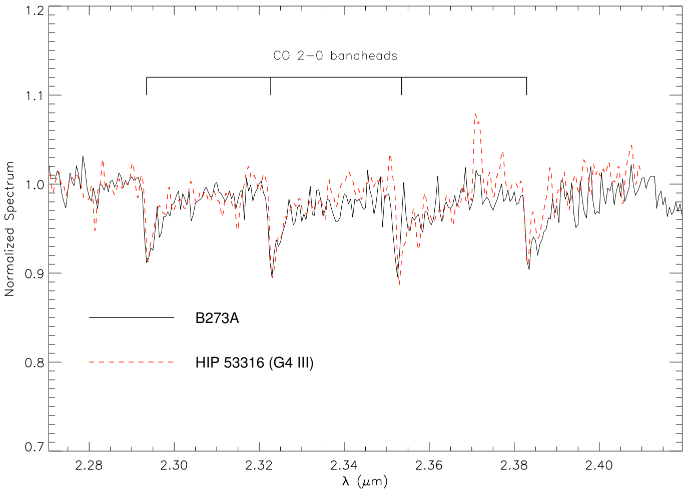

Fig. 13. Normalized SINFONI spectrum of B273A (black) in the wavelength range 2.27 – 2.42 μm, covering CO 2 – 0 handhead absorption. For comparison, the reference spectrum of mid-G giant HIP 53316 (SpT G4 III; Wallace & Hinkle 1997) is shown in red. The reference spectrum (R ∼ 3000) has been smoothed to the spectral resolution of SINFONI spectrum.

4.5. Extinction and Luminosity

In order to place IRS5A and B273A in the Hertzsprung-Russel diagram (HRD), one has to determine their luminosity. In principle, the already constrained spectral type of the source would give some hints to derive the extinction toward the source, because the temperature-dependent intrinsic color is reddened by a certain amount of extinction to the observed color. For instance, a general manner of determining the extinction for B stars is applying the short wavelength colors (e.g. $V-R$ vs $I-R$) rather than the near-IR colors (i.e., $J - H$ vs $H - K$), on consideration that the former ones are more sensitive to the temperatures of early-type stars. In the cases of YSOs, the short wavelength colors are the only reliable way to derive the extinction value because the near-IR colors are usually affected by the strong near-IR excess emission which is emitted by the hot circumstellar material.

The absence of hydrogen emission lines in the spectra of IRS5A and B273A suggests that there is no substantial accretion activity. We speculate that the $J - H$ color is not severely affected by dust thermal emission due to the absence of hot accretion tunnel flows. Following the extinction law at near-IR from Cardelli et al. (1989) and the specific value of $R_V = 3.9$ toward M 17 from Hoffmeister et al. (2008), the A_V values of IRS5A and B273A are estimated from their apparent $J - H$ colors on the basis of the intrinsic $J - H$ colors at certain temperatures (Pecaut & Mamajek 2013). The reliability of the obtained extinction is tested by reddening a blackbody of the proper temperature with the same A_V value. Note that the Cardelli et al. (1989) near-IR extinction law is invalid in the 5 – 20 μm range, hence the extinction law used by Robitaille et al. (2007) that works in the 1 – 20 μm range is employed when reddening the SEDs. In the 1 – 3 μm range, the extinction law used by Robitaille et al. (2007) is equivalent to the Cardelli et al. (1989) extinction law when $R_V = 3.1$. The reddened blackbody is shown in blue in Fig. 14. The blue blackbody curve matches the bluer part of the stellar SED for both objects. On the other hand, IRS5A displays a deep 9.7 μm silicate absorption feature. Using the empirical relation for silicate optical depth $A_V = (18 \pm 1)\,\tau_{9.7}$ (Whittet 2003), IRS5A's A_V is estimated as $\sim$ 41 mag from $\tau_{9.7} \sim 2.3$. Note that A_V of IRS5A is even higher than that ($\sim$ 40 mag) of UC1 (N+07), while the latter is redder than the former. Such a contradiction even could not be explained by the difference in spectral type between them. Alternatively, if we adopt $A_V/\tau_{9.7} = 9 - 19$ (Roche & Aitken 1985), A_V of IRS5A is hence between 21 – 44 mag. The A_V based on $\tau_{9.7}$ has a large error which originates from the various $A_V/\tau_{9.7}$ ratios. The A_V value of IRS5A calculated from its $J - H$ color agrees with the upper limit from optical data. IRS5A and B273A's A_V values derived by their $J-H$ colors are adopted in this paper (see Table 5).

The visual extinction A_V evaluated above is then converted to A_J at J-band following the relation $A_J \approx 0.27\,A_V$ when $R_V = 3.9$. Further, the J-band absolute magnitude (M_J) can be estimated for both IRS5A and B273A through distance modulus. For IRS5A, the value of M_J is -3 mag. Referring to Pecaut & Mamajek (2013), the temperature of IRS5A ($\sim$ 15000 K) corresponds to a J-band bolometric correction factor (BC$_J$) of -1.6 mag. Hence, the bolometric magnitude, $M_{\rm bol}$, of IRS5A is estimated to be -4.6 mag, corresponding to a bolometric luminosity $\approx 5500\,L_\odot$. Here the solar $M_{\rm bol}$ is adopted as +4.75 mag. Similarly, we have $M_J \approx -1.0$ mag, and BC$_J \approx 1.25$ for B273A ($T_{\rm eff} \sim 5200$ K). $M_{\rm bol} \approx 0.25$ of B273A is equal to a bolometric luminosity of 63 $L_\odot$.

The flux measurements from near- to mid-IR wavelengths provide an observational approach to evaluate the luminosity. With the new flux measurements in the 1 – 20 μm range presented in this paper, we are able to update the IR luminosity of IRS5A, and derive the IR luminosity for IRS5C and B273A. As shown in Fig. 14, we employ the simple blackbody curve to fit the infrared flux of the three objects. The significant absorption dip around 10 μm in IRS5A's SED corresponds to the 9.7 μm silicate absorption which is confirmed by the TIMMI2 spectrum. Hence the flux measurements at wavelengths around 9.7 μm are not used in fitting the SED of IRS5A. However, for the SEDs of IRS5C and B273A, because the 11.85 μm flux is the only available measurement in mid-IR, we still use this flux measurement in fitting. The 9.7 μm silicate absorption should be taken into account when dereddening the SED. Be aware of that the 11.85 μm flux is affected by the 9.7 μm silicate absorption feature, thus the blackbody fitting will overestimate the color temperatures of IRS5C and B273A.

The SED of IRS5A can be well fitted by two blackbody components with color temperatures of 1204 K and 264 K. The cooler component indicates a large amount of dust grains along the LOS of IRS5A. The color temperatures of IRS5C and B273A are 496 K and 1218 K, respectively. The observed IR luminosity in the 1 – 20 μm range, $L_{\rm IR}$, of these objects are summarized in the third column of Table 5.

IRS5A's $L_{\rm IR}$ is very close to the values in N+01 and K+02, which reported values of 3000 $L_\odot$ and 2600 $L_\odot$ for IRS5, respectively. In their work, the aperture size is larger than the one used in this paper, and IRS5C is not resolved in their larger beam infrared images. A smaller luminosity derived for IRS5A in this paper is reasonable. On the other hand, the observed $L_{\rm IR}$ of IRS5A and B273A are much lower than their bolometric luminosity $L_{\rm bol}$ derived above. If the observed flux measurements are extrapolated to longer and shorter wavelengths, and are corrected for the extinction, the $L_{\rm bol}$ of IRS5A and B273A can be constrained observationally.

The extinction-corrected $L_{\rm IR}$ is obtained for IRS5A and B273A by using the proper extinction law mentioned above. Furthermore, the $L_{\rm bol}$ of IRS5A and B273A are derived by extrapolating the best-fitting blackbody to longer and shorter wavelengths, e.g. in the range 0.02 – 200 μm. The obtained $L_{\rm bol}$ is listed in the fourth column of Table 5.

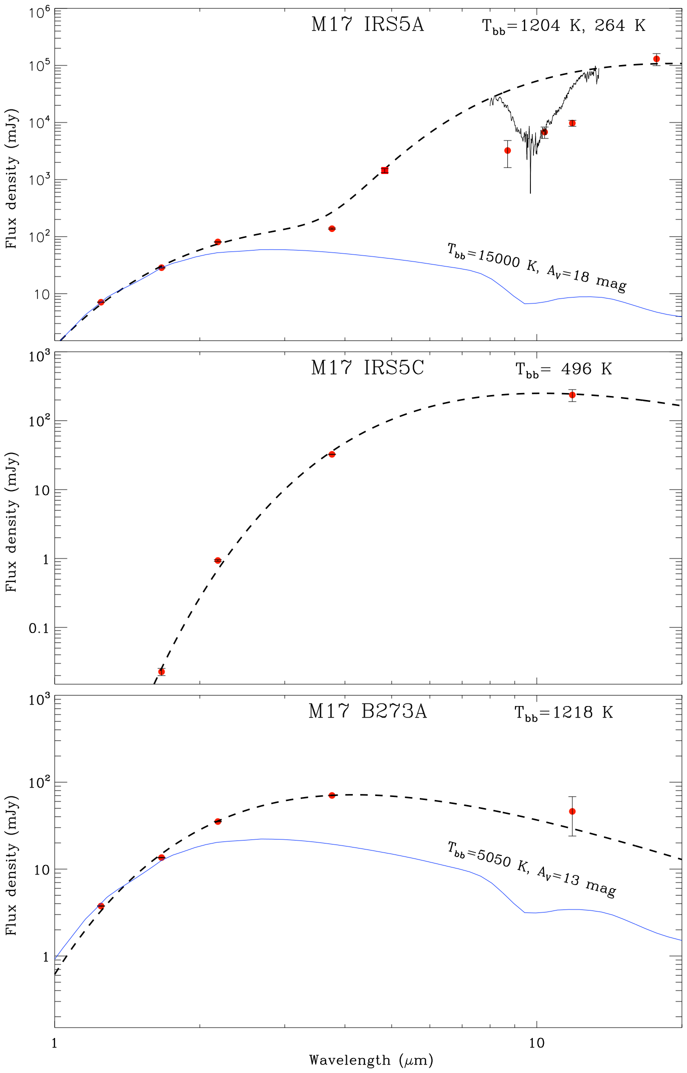

Fig. 14. SEDs constructed based on the flux measurements summarized in Table 2 and Table 3 (filled circles), and the M-band point by ISAAC (filled square; Hoffmeister 2008). For IRS5A, the TIMMI2 spectrum at around 9.7 μm is denoted by the solid curve in the top panel. The temperature of the blackbody (in blue) corresponds to the proper spectral type according to Cox (2000).

The $L_{\rm bol}$ of IRS5A and B273A derived from SED fitting are compared with the values obtained from the temperature-dependent bolometric correction values. For IRS5A, the former value is significantly larger than the latter one. This difference is partly caused by the extinction used in dereddening the SED of IRS5A. IRS5A shows evidence of circumstellar material, the extinction caused by the circumstellar material is included when dereddening the SEDs. However, the circumstellar extinction does not attenuate the $L_{\rm bol}$, but just redistributes the SED because the circumstellar material absorbs the blue photons and reemits at longer wavelengths if assuming an ideal blackbody. In the case of IRS5A, the circumstellar extinction might be a small portion of the total extinction, upon the consideration that the foreground extinction toward the southwestern bar is suggested to be on the order of 10 mag or even higher (e.g. Pellegrini et al.

Table 5. Infrared luminosity of the YSOs in the M 17 UC1 – IRS5 region

Object	A_V (mag)	L_{IR}[a] ($L_\odot$)	L_{bol} ($L_\odot$)
M 17 B273A	13	10 (44)	71
M 17 UC1[b]	40	2.5×10^3 (1.1×10^4)	3.0×10^4
M 17 IRS5A	18	2.0×10^3 (3.0×10^3)	8.6×10^3
M 17 IRS5C	-	13	-

Notes.
[a] Values in brackets are extinction-corrected L_{IR}.
[b] Values adopted from N+07.

2007; Sheffer & Wolfire 2013). We recalculated the L_{bol} with a smaller A_V value by 1 mag difference, and got smaller L_{bol} of $5.8\times10^3\,L_\odot$ for IRS5A, which agrees much better with the value of $5.5\times10^3\,L_\odot$. Therefore, we take the L_{bol} values in Table 5 as the upper limits, and the extinction-corrected L_{IR} as the lower limits in the following discussions.

5. Discussion

5.1. Multiplicity

With the high angular resolution infrared images toward M 17 UC1 – IRS5 region, the companions of the luminous infrared objects (IRS5, B273) are resolved for the first time. According to the *HKL* color-color diagram, the two components of the B273 system both show *L*-band excess emission. Thus, we suggest that B273A and B273B form a young binary system with a projected separation of about 2200 AU. Three of the five components of IRS5 show *L*-band excess emission. In light of IRS5D's position in Fig. 2, we also regard it as a member of IRS5 system taking into account the photometric errors, and suggest IRS5 might be a young quadruple system.

5.2. Structures of the circumstellar material

The large mid-IR excess emission of IRS5A and UC1 previously reported by N+01 and K+02 indicate circumstellar material for both objects. In addition, from a near-IR polarization view (CZ+12), the high-level polarization individually associated with IRS5A and UC1 also traces dust grains physically linked with the two objects. Specifically, the almost edge-on circumstellar disk of UC1 found by N+07 produces the high-level K_s-band polarization vectors parallel to the disk. The polarization pattern of the IRN illuminated by IRS5A, however, implies a quite different orientation than UC1. E.g. the inclination angle of IRS5A's IRN estimated in CZ+12 is $\sim 50^\circ$ from the plane of the sky.

Fig. 9 presents perfect geometric match between the H_2 emission and polarized light, which explains the physical carriers of the polarized light. The H_2 emission residing just beside UC1 is exactly aligned with the elongated feature extending to northwest, which is suggested to coincide with the dust thermal emission originated in the circumstellar disk of UC1 (see Sect. 4.2). We speculate that such H_2 emission is related with the circumstellar disk of UC1, and actually traces the warm H_2 gas in UC1's disk. The dust grains in UC1's disk scatter the incident starlight, and produce the polarized light seen at near-IR. The H_2 emission filament related to UC1's disk is one of the three H_2 emission filaments that are parallel to each other, and parallel to the IF. The H_2 filament at the midway between the IF and UC1 is spatially coinciding with the bar-like emission feature seen in the NACO/*K* image (see Sect. 4.1.2 and Fig. 3). Moreover, the area covered by this bar-like emission in turn is also occupied by the south-north mid-IR extended emission originated from UC1. This south-north extended emission seen in mid-IR and the coordinated IRN seen in near-IR polarized light together suggest a south-north outflow from UC1. The bar-like emission seems to arise at the northeastern side of this outflow because this side is facing to the IF. The IF northeast of the outflow suppresses the outflowing material on the northeastern side, and consequently forms a sheet of gas with higher temperature than the rest of the outflow. The temperature difference between the sheet at outflow's northeastern side and the rest of the outflow explains well the different morphology of the outflow seen between near-IR and mid-IR wavelengths. Moreover, the coordinated emitting H_2 gas at the northeastern side of the outflow is suggested to be excited at a temperature of $\sim$ 600 K (see Sect. 4.3.3), while the rest of the outflow is suggested to have thermal temperature around 100 K heated by an early-B outflow driving object (Longmore et al. 2011). The north-south outflow of UC1 is most likely the blue-shifted lobe, with the red-shifted lobe invisible because of the severe attenuation.

The coordinated emitting H_2 gas surrounding IRS5A and the IRN illuminated by the same object indicates a distribution of gas and dust embracing IRS5A in the north with an arc-like shape. The circular shape of the IRN illuminated by IRS5A reminds us that the southern half would be associated with H_2 gas either, although the southern half is not fully covered by the SINFONI data in its small FOV. The temperature of this material distribution is $\sim$ 600 K, similar to the associated emitting H_2 gas. With the high-resolution VISIR 11.85 μm image, we expect a tight relation between the diffuse mid-IR emission and the IRN, just like what has been observed for UC1. However, the diffuse mid-IR emission is only observed at the midway between IRS5A and UC1, where merely a portion of the IRN is spatially associated (see Sect. 4.2). Indeed, this mismatch can be the result of two separate material distributions that are just along the same LOS; the dust temperature responsible for the mid-IR emission of IRS5A is modeled to be around 264 K, while the dust temperature linked with the IRN and H_2 emission is fitted to be around 575 K. The two lobes in the core region of IRS5A stack with the inner circle of the arc-like material along the LOS. The different morphology of IRS5A seen at near-IR and mid-IR rise the question if the mid-IR emission comes from the area close to IRS5A, or from its envelope or outflow. The dark lane separating the two mid-IR lobes can be somehow explained by a nearly edge-on cold disk that absorbs the mid-IR emission from backside. The proposed cold disk should have impacts at near-IR bands, such as a silhouette dividing the object into two lobes as well, very similar to UC1. Nevertheless, IRS5A's near-IR images do not show any sign of silhouette disk. The extinction of IRS5A is another strong issue against the assumption of a nearly edge-on cold disk, because the circumstellar extinction is only a small portion of the total extinction of IRS5A. We propose that the mid-IR emission actually arises from the outflow whose axis is almost along the LOS of IRS5A. The two lobes seen in mid-IR correspond to the outflow walls at two sides. In view of the severe attenuation at near-IR bands and at around 10 μm (Chapman et al. 2009), the H_2 emission filament is the blue-shifted lobe. Meanwhile the outflowing material traced by the mid-IR emission might be blue-shifted, because of the attenuation issue too.

We note from Fig. 8 that IRS5C is closely associated with H_2 1−0 S(1) emission. Indeed, IRS5C is embraced by H_2 1−0 S(1)

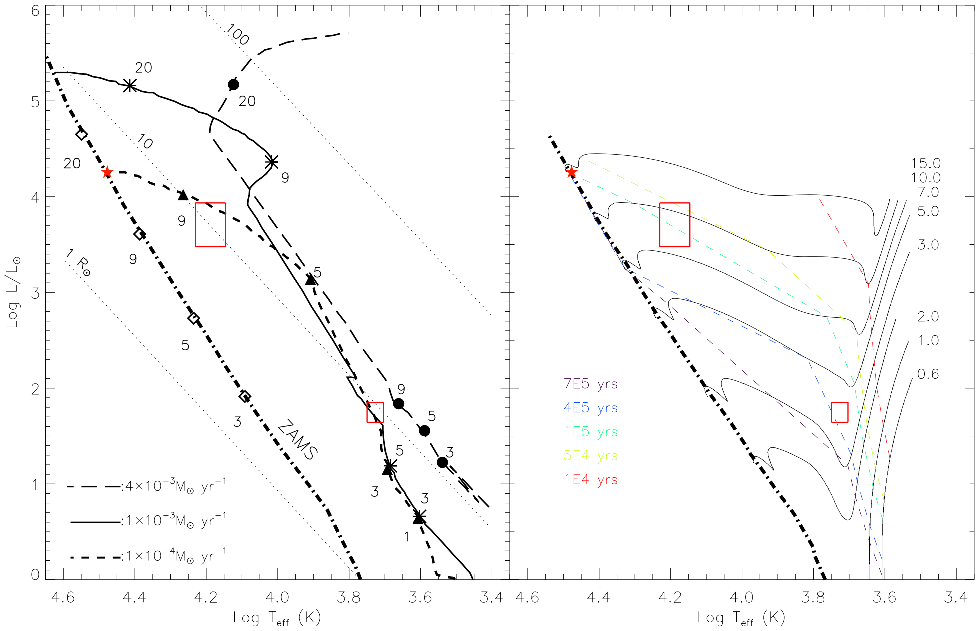

Fig. 15. Positions of the YSOs in the HRD with well constrained temperatures and luminosities. Red rectangles outline the parameter space of IRS5A (the upper one) and B273A (the lower one), and the red asterisk at upper left marks UC1. For IRS5A and B273A, the conversion from spectral types to effective temperatures and bolometric luminosities is referred to Sect. 4.5, while UC1 is assumed to be a ZAMS B0.5 star in light of the HCHII region (N+07 and references therein). Left panel: positions of the YSOs compared with the model of massive star formation via disk accretion (H+10). The symbols along the evolutionary loci at various accretion rates and the ZAMS locus denote the mass at each position. Right panel: positions of the YSOs placed against the PMS evolutionary tracks of different masses (CA+12). Isochrones of five ages are drawn as the dashed lines in different colors.

emission which shows an elliptical shape orientated at P.A. ∼ 65°. The bulk of H_2 emission is shifted northeast to IRS5C. As described in Sect. 4.1.1, IRS5C is coinciding with 22-GHz H_2O maser which is located 0.″5 northwest to IRS5C. The H_2 1−0 S(1) emission associated with IRS5C resembles that found for some Herbig Ae/Be stars in their circumstellar disks, where molecular H_2 gas is heated by the Ae/Be stars themselves (Carmona et al. 2011). The strong excess emission at *L*-band (this work) and mid-IR indicates the presence of circumstellar material surrounding IRS5C. Hence it is plausible that H_2 gas among the warm circumstellar material thermally emits H_2 1−0 S(1) emission detected here. However, unlike the H_2 1−0 S(1) emission detected in the circumstellar disks of HD 97048 and HD 100546 which originates at radii on the order of $\sim 10^1 - 10^2$ AU, the size of the H_2 1−0 S(1) emission associated with IRS5C is about 1600 AU in diameter. H_2 emission occurring at large distances requests massive stars other than Herbig Ae/Be stars to maintain sufficient radiation field. Nevertheless, the other possibility is that the H_2 emission is externally excited by the FUV photons from the ionizing OB stars in M 17. In light of the excitation mechanism of the H_2 emission associated with other objects, the latter explanation is more plausible and reliable. To explain the location of the H_2 emission, we propose a nearly edge-on flared disk with radius of 1600 AU to approximately match the shape of H_2 emission. In addition, the 22-GHz H_2O maser resides 0.″5 away along the axis of the circumstellar disk of IRS5C. In some cases, the H_2O masers can be excited in the shock fronts where the outflowing gas from high-mass YSO strongly interacts with the surrounding molecular gas (e.g. Torrelles et al. 2014). Considering the position of the H_2O maser with respect to the proposed disk, and the disk's size, we interpret that IRS5C is a deeply embedded high-mass protostar with a nearly edge-on flared disk. IRS5C does not show radio free-free emission at 1.3 cm (Johnson et al. 1998), which implies that IRS5C is still at an early stage.

5.3. Evolutionary Stages of YSOs

With the known temperature and luminosity for IRS5A and B273A, the locations of these two objects in the HRD will reveal their evolutionary stages when compared with numerical models for star formation. The model of H+10 specifically considers the evolution of a massive protostar via disk accretion, while that of Claret (2012) models the PMS evolution purely tuned by the gravitational contraction without mass feeding, i.e. non-accretion model.

Both models indicate that IRS5A is still experiencing PMS stage. Using the accretion model H+10 to estimate IRS5A's mass and age is problematic, due to the constant accretion rate and fixed initial condition used in H+10. If referring to the non-accretion PMS model, IRS5A's mass is currently about 9 $M_{\odot}$ and will not change much when IRS5A is evolving toward ZAMS. And a non-accretion 0.1 Myr isochrone passes by IRS5A's position in the HRD. Note that non-accretion model simplifies the evolution of protostars, whose accretion histories, initial radii and thermal efficiencies can strongly alter their positions in the HRD. Nevertheless, very young age estimates (< 1 Myr) for stars hotter than 3500 K based on non-accretion model are reliable (Hosokawa et al. 2011). Therefore, we suggest that the age estimate for IRS5A is reliable.

However, the circumstellar material encircling IRS5A that is found to be the bipolar molecular outflow driven by itself, and the lack of accretion tracers both doubt that IRS5A would continue accretion to gain mass. The peculiarity of this object is that it currently does not show any tracer of accretion funnel flow, which imply either periodic accretion or feedback (radiation pressure, outward mass flow) halted accretion. Both mechanisms are thought to have impact on the final mass of high-mass protostar, hence are crucial to understand the formation of high-mass protostar. Otherwise, the detection limit of the SINFONI data could also prevent resolving weak hydrogen emission lines (see the discussion in Sect. 5.4). Follow-up investigations for the gas kinematic in the close vicinity of IRS5A will contribute to determine the gas motion and consequently clarify the evolution trend via constraining the accretion status. Such follow-up studies need high spatial resolution and high spectral resolution observations, which can be implemented by ALMA (Atacama Large Millimeter/submillimeter Array).

B273A is located in the right-lower area of HRD. Model H+10 interprets mass gaining for B273A, however, it seems to lack hydrogen recombination lines. The excess emission at L-band and mid-IR both indicate the presence of circumstellar material, e.g. a circumstellar disk. Hence, we propose phases of periodic accretion or halted accretion for B273A, while the emission line strength below the detection limit could be plausible too. In the other case, the location of B273A in the right panel of Fig. 15 suggests a mass $\sim 4\,M_\odot$ and an age $\sim 4 \times 10^5$ yrs. As a similar case to IRS5A, we believe that B273A's age estimate based on the non-accretion PMS model is reliable, and B273A is still at the first-half stage of its entire evolution life toward ZAMS.

5.4. Feedback on accretion

One may argue that the spectra of IRS5A and B273A have a low resolution ($R \sim 1500$) and not high enough S/N, which leads to the 'fake' non-detection in case of weak Brγ emission. Based on the spectral resolution (FWHM $\approx$ 3 pixels) and continuum's noise level, we estimated that the upper limit of Brγ emission flux is $\sim 2.2 \times 10^{-15}\,\mathrm{ergs\,cm^{-2}\,s^{-1}}$ for IRS5A, and $7.9 \times 10^{-16}\,\mathrm{ergs\,cm^{-2}\,s^{-1}}$ for B273A; with the extinction values of this two objects shown in Table 5, the extinction-corrected Brγ line flux, $f_{\mathrm{Br}\gamma}$, is $\sim 1.3 \times 10^{-14}\,\mathrm{ergs\,cm^{-2}\,s^{-1}}$ for IRS5A, and $\sim 2.8 \times 10^{-15}\,\mathrm{ergs\,cm^{-2}\,s^{-1}}$ for B273A. Further the luminosity of Brγ emission line was computed as $L_{\mathrm{Br}\gamma} = 4\,\pi\,d^2\,f_{\mathrm{Br}\gamma}$, where d is the distance of M 17. The Brγ line luminosity is found to be tightly correlated with the accretion luminosity, L_{acc}, for a statistical sample of low-mass YSOs (e.g. Mendigutía et al. 2011; Rigliaco et al. 2012; Alcalá et al. 2014). For high-mass YSOs, the correlation between $L_{\mathrm{Br}\gamma}$ and L_{acc} is not well established due to the lack of a statistics meaningful sample. As an approximation, we used the $\log L_{\mathrm{Br}\gamma} - \log L_{\mathrm{acc}}$ relation reported in Alcalá et al. (2014) to estimate the L_{acc}, which is $\sim 2.2\,L_\odot$ for IRS5A, and $\sim 0.38\,L_\odot$ for B273A. From the positions of this two objects in the HRD, we estimated a radius of $\sim 10\,R_\odot$ for both of them. Together with the masses of the two objects mentioned above, the formula

$$\dot{M}_{\mathrm{acc}} \approx 1.25\,\frac{L_{\mathrm{acc}}\,R_*}{G\,M_*}$$

gives the upper limit of $\dot{M}_{\mathrm{acc}}$, which is $\sim 1.1 \times 10^{-7}\,M_\odot\,\mathrm{yr}^{-1}$ for IRS5A, and $\sim 3.8 \times 10^{-8}\,M_\odot\,\mathrm{yr}^{-1}$ for B273A.

High-mass stars can arrive at ZAMS stage still during their accretion phase. However, the enormous radiation pressure and ionizing photons will act on the accretion flow and dissipate the circumstellar material. Thus, the timescale of the accretion phase for a high-mass protostar will strongly depend on the stellar mass, which in turn is constrained by accretion rate. Such timescale is far to be known for high-mass protostars. UC1's disk suggests that this B0.5 ZAMS star might be still in its accretion phase. A plausible evidence supporting accretion comes from the Brγ emission at the position of UC1's southwest lobe (Fig. 5). Nevertheless, Brγ emission can be produced in the HCHII region associated with UC1. For an HCHII region, the dynamics and morphology of the ionized gas are determined by the ratio of the ionization radius, R_i, and the gravitational bound radius, R_b, defined by $G\,M_*/2\,c_s^2$, where M_* is the stellar mass and c_s is the sound speed (Keto 2007). With $M_* = 15\,M_\odot$ and $c_s = 10\,\mathrm{km\,s^{-1}}$ (at the temperature of 10^4 K for ionized gas), R_b is 66 AU. Since the Brγ emission must come from the ionized gas of the HCHII region, the Brγ line map in Fig. 5 shows the morphology of the HCHII region around UC1. The distance from the obscured centroid of UC1 to the southwestern Brγ emission knot is taken as the value of R_i, which is $\sim 0\farcs25$, or ~ 500 AU. Thus, for UC1, $R_i \gg R_b$, corresponding to a stage of HCHII region that the ionized gas moves outward to form an outflow (Keto 2007). In this picture, the accretion is confined to a narrow range of angles close to the mid-plane of the disk and is close to termination. Without the observational evidence of the gas dynamics in the inner most region of UC1, the accretion status of UC1 is controversial.

Due to the large inclination angle of IRS5A from the plane of the sky, near-IR emission lines produced in the accretion flow (if exists) can be seen without the severe attenuation by the disk. In fact, IRS5A does not show any emission line indicating accretion. We have proposed two reasons for the absence of accretion indicators in Sect. 5.3. If in the case of non-accretion phase, the evolutionary stage of IRS5A would imply that accretion could even be halted before high-mass protostar arriving at ZAMS. In view of the lower temperature at the early stage of high-mass protostar, radiation feedback is not as strong as for a ZAMS star, thus outflow activities are additionally required to be responsible for the reversed accretion. In a large picture, the expanding H II region of M 17 might also contribute to the dissipation of accretion tunnel flows. The deduced timescale of accretion phase is thus $\sim 1 \times 10^5$ yrs, on the same order of high-mass protostar's age. On the other hand, the probable periodic accretion process of IRS5A would suggest a timescale of accretion phase much longer. The determination of the gas dynamics in the inner most area of IRS5A will disentangle this confusing puzzle.

Interestingly, the absence of hydrogen recombination lines in B273A's spectrum implies a terminated-accretion phase. An intermediate-mass YSO with an age $\sim 4 \times 10^5$ yrs like B273A is most likely to show accretion activity, because YSOs at later evolutionary stages such as intermediate-mass T Tauri stars ($1.5 - 4\,M_\odot$, $1 - 10$ Myr) were observed to show Brγ emission even in low-resolution ($R \sim 800$) near-IR spectra (Calvet et al. 2004). This discrepancy between the observation and the predication for B273A indicates additional feedback to dissipate the accretion funnel flows. The exact spatial coincident between B273A and the IF implies that the expanding H II region driven by the ionizing photons is the plausible mechanism of external feedback.

From the current masses and ages of these two objects, IRS5A and B273A require mass accretion rate of $9 \times 10^{-5}\,M_\odot\,\mathrm{yr}^{-1}$ and $1{\times}10^{-5}\,M_\odot\,\mathrm{yr}^{-1}$, respectively. Even in the possibility of weak Brγ, we still note a dramatically drop of $\dot{M}$ for both objects. This could be also the result of feedback from stellar activities and expanding H II region. For the two low-mass YSOs, B273B and IRS5B, we could similarly estimate that the upper limit of their mass accretion rates is definitely lower than that of B273A , i.e. $\sim 3.8{\times}10^{-8}\,M_\odot\,\mathrm{yr}^{-1}$. The typical mass accretion rate of low-mass YSOs is on the order of $1 \times 10^{-8}\,M_\odot\,\mathrm{yr}^{-1}$ (e.g. Fang et al. 2013; Alcalá et al. 2014), which is comparable to the detection limit of B273B and IRS5B's spectra. The lack of Brγ emission line in the spectra of low-mass YSOs (e.g., B273B, IRS5B) is reminiscent of non-accretion phase, however, we cannot rule out the possibility that their accretion indicators could be revealed by higher resolution spectroscopic observation. In the case of non-accretion phase for these low-mass YSOs, it seems to remind us that such external radiation feedback might be important in the disk clearing process for the YSOs in massive star forming regions.

5.5. Properties of M 17 SW

Previous studies of M 17 SW speculated that a dense PDR with high-density clumps and low-density gas to match the observed properties of M 17 SW (Meixner et al. 1992; Pérez-Beaupuits et al. 2010, 2012). However, these studies are based on far-IR and radio line observations, and thus cannot resolve structures smaller than several arcseconds. The near-IR H_2 emission detected in the M 17 UC1 – IRS5 region with extremely high spatial resolution (100 mas) set a entirely new picture for the warmest part of M 17 SW. The column densities of several H_2 $v = 1 - 0$ ro-vibrational lines show that H_2 gas mostly concentrates in filaments in the range 0.02 – 0.05 pc. The H_2 line ratios, as been discussed in Sect. 4.3.3, refer to a gas density of $> 10^5\,\mathrm{cm}^{-3}$ if they are compared to PDR models (Burton et al. 1990). The high-density nature of M 17 SW is also evidenced by the molecular gas persisting just west of the IF (Pérez-Beaupuits et al. 2012). This can be interpreted as the result of self-shielding of molecules in high-density PDR which can move the transition regions for H I/H_2 close to the surface of the cloud (Burton et al. 1990). Complementally, the H_2 gas temperature characterized by the ro-vibrational diagram is in the range 500 – 750 K. In contrast, H I observations toward M 17 specifically showed that H I number density toward the M 17 UC1 – IRS5 region is in the range $3.7 \times 10^3 - 1.5 \times 10^4\,\mathrm{cm}^{-3}$, which corresponds to H I spin temperature between 50 K and 200 K in many directions toward M 17 (Brogan et al. 1999). Therefore, the H_2 filaments presented here confirm for the first time that dense clumps with number density two orders of magnitude higher and temperatures higher than ambient atomic gas can exist down to 10^{-2} pc scale inside a dense PDR like M 17 SW, which was previously suggested being clumpy (Meixner et al. 1992).

6. Summary and conclusions

In this paper we presented diffraction-limited near- to mid-IR images and SINFONI integral field spectroscopy at $H + K$ toward the M 17 UC1 – IRS5 region, which shows emission lines of He I, H I, and H_2. Our diffraction-limited data reveal new fine structures of this region.

1. This work complements the work by CZ+12 from a view of much higher angular resolution. The IRN identified in CZ+12 illuminated by IRS5A and by UC1 are confirmed to trace the molecular outflow driven by the two objects, respectively. Combining the SINFONI H_2 line emission map and the mid-IR VISIR image, a blue-shifted outflow lobe is proposed for IRS5A, with two types of tracers in the form of H_2 emission filament and mid-IR emission. The molecular outflow UC1 is running south-north with its blue-shifted lobe merely visible in forms of near-IR polarized light and mid-IR emission. The northeastern side of UC1's outflow is suppressed by the shock fronts driven by the expanding H II region. Thus a sheet of warm, dense gas forms at the northeastern edge of UC1's molecular outflow, and appears in forms of the bar-like emission seen in K-band and the H_2 emission filament which are both parallel to the ionization front.

2. The uniform line ratios of all H_2 emitting areas indicate the same excitation mechanism; the H_2 molecules are initially pumped by FUV photons, and are repopulated by the collisional deexcitation in a dense PDR. The H_2 gas excitation temperature is estimated to be around 575 K based on the ro-vibrational diagram of the detected H_2 $v = 1$ lines. The H_2 line ratios are used to probe the properties of the PDR. Comparisons to PDR models suggest clumpy PDR structure with at least two components: warm, dense molecular clumps with $n_\mathrm{H} > 10^5\,\mathrm{cm}^{-3}$ and $T \sim 575$ K and atomic gas with $n_\mathrm{H} \sim 3.7\times10^3 - 1.5\times10^4\,\mathrm{cm}^{-3}$ and $T \sim 50 - 200$ K.

3. IRS5 might be a young quadruple system containing IRS5A, IRS5B, IRS5C, and IRS5D. Its primary star IRS5A is classified as a B3–B7 V/III star with a bolometric luminosity of $3.0 - 8.6\times10^3\,L_\odot$, confirmed to be a high-mass protostar with mass $\sim 9\,M_\odot$ and age $\sim 1 \times 10^5$ yrs, while the three lower mass companions are much less constrained. Particularly, IRS5C might be a deeply embedded high-mass protostellar object with a dusty disk. The spectral type of B273A is assigned to G4/5 III, suggesting an intermediate-mass YSO of $\sim 4\,M_\odot$ and an age $\sim 4 \times 10^5$ yrs when compared with the non-accretion PMS model. B273A may have a lower mass companion B273B of possibly similar age.

4. The Brγ emission of UC1 is ambiguous for tracing the accretion because the emission can arise from the HCHII region as well; UC1 might have terminated accretion from a concern on the ratio of $R_i \gg R_b$. The absence of Brγ emission in the SINFONI spectra of the other YSOs of various masses implies terminated accretion for them. Even in the case of weak Brγ emission that cannot be resolved by the SINFONI data, the steep drop in the accretion rates of IRS5A and B273A along the protostellar evolution suggests processes of dissipating accretion funnel flows. The object IRS5A is unique because it is during a stage when its radiation feedback is not high enough to severely destroy accretion funnel flows or even to terminate the accretion; therefore, the expanding H II region and its bipolar outflow both are suggested to contribute simultaneously. For the other YSOs, the expanding H II region could be the major mechanism on dissipating/terminating accretion.

Acknowledgements. This work is supported by the Strategic Priority Research Program "The Emergence of Cosmological Structure" of the Chinese Academy of Sciences, grant No. XDB09000000. Z.J. acknowledges the support by NSFC 11233007. M.F. acknowledges the support by the NSFC through grants 11203081. Z.C. acknowledges Dr. S. Zhang for his IDL routines to make good-look RGB figures. This publication used data products from the Two Micron All Sky Survey, which is a joint project of the University of Massachusetts and the Infrared Processing and Analysis Center/California Institute of Technology, funded by the National Aeronautics and Space Administration and the National Science Foundation. This research made use of the SIMBAD database, operated at the CDS, Strasbourg, France. This research made use of NASA's Astrophysics Data System Bibliographic Services.

References

Alcalá, J. M., Natta, A., Manara, C. F., et al. 2014, A&A, 561, A2

Allers, K. N., Jaffe, D. T., Lacy, J. H., Draine, B. T., & Richter, M. J. 2005, ApJ, 630, 368
Bik, A., Kaper, L., Hanson, M. M., & Smits, M. 2005, A&A, 440, 121
Bik, A., Puga, E., Waters, L. B. F. M., et al. 2010, ApJ, 713, 883
Blum, R. D. & McGregor, P. J. 2008, AJ, 135, 1708
Breen, S. L., Caswell, J. L., Ellingsen, S. P., & Phillips, C. J. 2010, MNRAS, 406, 1487
Brogan, C. L. & Troland, T. H. 2001, ApJ, 560, 821
Brogan, C. L., Troland, T. H., Roberts, D. A., & Crutcher, R. M. 1999, ApJ, 515, 304
Burton, M. G., Geballe, T. R., Brand, P. W. J. L., & Moorhouse, A. 1990, ApJ, 352, 625
Calvet, N., Muzerolle, J., Briceño, C., et al. 2004, AJ, 128, 1294
Cardelli, J. A., Clayton, G. C., & Mathis, J. S. 1989, ApJ, 345, 245
Carmona, A., van der Plas, G., van den Ancker, M. E., et al. 2011, A&A, 533, A39
Casali, M. M. & Eiroa, C. 1996, A&A, 306, 427
Caswell, J. L. 1998, MNRAS, 297, 215
Caswell, J. L., Vaile, R. A., Ellingsen, S. P., Whiteoak, J. B., & Norris, R. P. 1995, MNRAS, 272, 96
Caswell, J. L., Yi, J., Booth, R. S., & Cragg, D. M. 2000, MNRAS, 313, 599
Chapman, N. L., Mundy, L. G., Lai, S.-P., & Evans, II, N. J. 2009, ApJ, 690, 496
Chen, Z., Jiang, Z., Wang, Y., et al. 2012, PASJ, 64, 110 (CZ+12)
Chen, Z., Nürnberger, D. E. A., Chini, R., et al. 2013, A&A, 557, A51
Chini, R., Nielbock, M., & Beck, R. 2000, A&A, 357, L33
Churchwell, E. 2002, ARA&A, 40, 27
Claret, A. 2012, A&A, 541, A113
Cox, A. N. 2000, Allen's astrophysical quantities
Dabrowski, I. 1984, Canadian Journal of Physics, 62, 1639
Ducati, J. R., Bevilacqua, C. M., Rembold, S. B., & Ribeiro, D. 2001, ApJ, 558, 309
Fang, M., van Boekel, R., Bouwman, J., et al. 2013, A&A, 549, A15
Fontani, F., Cesaroni, R., & Furuya, R. S. 2010, A&A, 517, A56
Gatley, I., Hasegawa, T., Suzuki, H., et al. 1987, ApJ, 318, L73
Gillessen, S., Davies, R., Kissler-Patig, M., et al. 2005, The Messenger, 120, 26
González-Fernández, C. & Negueruela, I. 2012, A&A, 539, A100
Grave, J. M. C. & Kumar, M. S. N. 2009, A&A, 498, 147
Hanson, M. M., Conti, P. S., & Rieke, M. J. 1996, ApJS, 107, 281
Hanson, M. M., Howarth, I. D., & Conti, P. S. 1997, ApJ, 489, 698
Hanson, M. M., Kudritzki, R.-P., Kenworthy, M. A., Puls, J., & Tokunaga, A. T. 2005, ApJS, 161, 154
Hanson, M. M., Rieke, G. H., & Luhman, K. L. 1998, AJ, 116, 1915
Hatch, N. A., Crawford, C. S., Fabian, A. C., & Johnstone, R. M. 2005, MNRAS, 358, 765
Hayashi, M., Hasegawa, T., Gatley, I., Garden, R., & Kaifu, N. 1985, MNRAS, 215, 31P
Hoffmeister, V. H. 2008, PhD thesis, Ruhr-Universität Bochum
Hoffmeister, V. H., Chini, R., Scheyda, C. M., et al. 2008, ApJ, 686, 310
Hoogerwerf, R., de Bruijne, J. H. J., & de Zeeuw, P. T. 2000, ApJ, 544, L133
Hosokawa, T., Offner, S. S. R., & Krumholz, M. R. 2011, ApJ, 738, 140
Hosokawa, T. & Omukai, K. 2009, ApJ, 691, 823
Hosokawa, T., Yorke, H. W., & Omukai, K. 2010, ApJ, 721, 478 (H+10)
Johnson, C. O., Depree, C. G., & Goss, W. M. 1998, ApJ, 500, 302
Kassis, M., Deutsch, L. K., Campbell, M. F., et al. 2002, AJ, 124, 1636 (K+02)
Keto, E. 2007, ApJ, 666, 976
Kumar, M. S. N. & Grave, J. M. C. 2007, A&A, 472, 155
Lada, C. J. & Adams, F. C. 1992, ApJ, 393, 278
Lagage, P. O., Pel, J. W., Authier, M., et al. 2004, The Messenger, 117, 12
Lenzen, R., Hartung, M., Brandner, W., et al. 2003, in Society of Photo-Optical Instrumentation Engineers (SPIE) Conference Series, Vol. 4841, Instrument Design and Performance for Optical/Infrared Ground-based Telescopes, ed. M. Iye & A. F. M. Moorwood, 944–952
Longmore, S. N., Pillai, T., Keto, E., Zhang, Q., & Qiu, K. 2011, ApJ, 726, 97
Luhman, K. L., Engelbracht, C. W., & Luhman, M. L. 1998, ApJ, 499, 799
Lumsden, S. L., Puxley, P. J., & Hoare, M. G. 2001, MNRAS, 328, 419
Martín-Hernández, N. L., Bik, A., Puga, E., Nürnberger, D. E. A., & Bronfman, L. 2008, A&A, 489, 229
Meixner, M., Haas, M. R., Tielens, A. G. G. M., Erickson, E. F., & Werner, M. 1992, ApJ, 390, 499
Meixner, M. & Tielens, A. G. G. M. 1993, ApJ, 405, 216
Mendigutía, I., Calvet, N., Montesinos, B., et al. 2011, A&A, 535, A99
Meyer, M. R., Calvet, N., & Hillenbrand, L. A. 1997, AJ, 114, 288
Molinari, S., Pezzuto, S., Cesaroni, R., et al. 2008, A&A, 481, 345
Murphy, T., Cohen, M., Ekers, R. D., et al. 2010, MNRAS, 405, 1560
Nielbock, M., Chini, R., Hoffmeister, V. H., et al. 2007, ApJ, 656, L81 (N+07)
Nielbock, M., Chini, R., Jütte, M., & Manthey, E. 2001, A&A, 377, 273 (N+01)
Nürnberger, D. E. A., Chini, R., Eisenhauer, F., et al. 2007, A&A, 465, 931
Okumura, S.-I., Mori, A., & Yanagisawa, K. 2004, PASJ, 56, 705
Pecaut, M. J. & Mamajek, E. E. 2013, ApJS, 208, 9
Pellegrini, E. W., Baldwin, J. A., Brogan, C. L., et al. 2007, ApJ, 658, 1119
Pérez-Beaupuits, J. P., Spaans, M., Hogerheijde, M. R., et al. 2010, A&A, 510, A87
Pérez-Beaupuits, J. P., Wiesemeyer, H., Ossenkopf, V., et al. 2012, A&A, 542, L13
Reimann, H.-G., Weinert, U., & Wagner, S. 1998, in Society of Photo-Optical Instrumentation Engineers (SPIE) Conference Series, Vol. 3354, Infrared Astronomical Instrumentation, ed. A. M. Fowler, 865–876
Rigliaco, E., Natta, A., Testi, L., et al. 2012, A&A, 548, A56
Robitaille, T. P., Whitney, B. A., Indebetouw, R., & Wood, K. 2007, ApJS, 169, 328
Roche, P. F. & Aitken, D. K. 1985, MNRAS, 215, 425
Rousset, G., Lacombe, F., Puget, P., et al. 2003, in Society of Photo-Optical Instrumentation Engineers (SPIE) Conference Series, Vol. 4839, Adaptive Optical System Technologies II, ed. P. L. Wizinowich & D. Bonaccini, 140–149
Sewilo, M., Churchwell, E., Kurtz, S., Goss, W. M., & Hofner, P. 2004, ApJ, 605, 285
Sheffer, Y. & Wolfire, M. G. 2013, ApJ, 774, L14
Sternberg, A. & Dalgarno, A. 1989, ApJ, 338, 197
Stutzki, J. & Guesten, R. 1990, ApJ, 356, 513
Stutzki, J., Stacey, G. J., Genzel, R., et al. 1988, ApJ, 332, 379
Tanaka, M., Hasegawa, T., Hayashi, S. S., Brand, P. W. J. L., & Gatley, I. 1989, ApJ, 336, 207
Torrelles, J. M., Trinidad, M. A., Curiel, S., et al. 2014, MNRAS, 437, 3803
Turner, J., Kirby-Docken, K., & Dalgarno, A. 1977, ApJS, 35, 281
Wallace, L. & Hinkle, K. 1997, ApJS, 111, 445
Whittet, D. C. B., ed. 2003, Dust in the galactic environment
Xu, Y., Moscadelli, L., Reid, M. J., et al. 2011, ApJ, 733, 25
Yorke, H. W. & Bodenheimer, P. 2008, in Astronomical Society of the Pacific Conference Series, Vol. 387, Massive Star Formation: Observations Confront Theory, ed. H. Beuther, H. Linz, & T. Henning, 189
Zinnecker, H. & Yorke, H. W. 2007, ARA&A, 45, 481